



**HAL**  
open science

## 3D Modeling of satellite spectral images, radiation budget and energy budget of urban landscapes

Jean-Philippe Gastellu-Etchegorry

► **To cite this version:**

Jean-Philippe Gastellu-Etchegorry. 3D Modeling of satellite spectral images, radiation budget and energy budget of urban landscapes. *Meteorology and Atmospheric Physics*, 2008, MAP-0/939, pp.1-21. 10.1007/s00703-008-0344-1 . ird-00405362

**HAL Id: ird-00405362**

**<https://ird.hal.science/ird-00405362>**

Submitted on 20 Jul 2009

**HAL** is a multi-disciplinary open access archive for the deposit and dissemination of scientific research documents, whether they are published or not. The documents may come from teaching and research institutions in France or abroad, or from public or private research centers.

L'archive ouverte pluridisciplinaire **HAL**, est destinée au dépôt et à la diffusion de documents scientifiques de niveau recherche, publiés ou non, émanant des établissements d'enseignement et de recherche français ou étrangers, des laboratoires publics ou privés.

Centre d'Etudes Spatiales de la BIOSphère Paul Sabatier University,  
CNES – CNRS, IRD, Toulouse Cedex, France

## 3D Modeling of satellite spectral images, radiation budget and energy budget of urban landscapes

J. P. Gastellu-Etchegorry

With 15 Figures

Received 16 April 2007; Accepted 27 October 2008

Published online • • 2008 © Springer-Verlag 2008

### 15 Summary

16 DART EB is a model that is being developed for simulating  
17 the 3D (3 dimensional) energy budget of urban and natural  
18 scenes, possibly with topography and atmosphere. It simu-  
19 lates all non radiative energy mechanisms (heat conduction,  
20 turbulent momentum and heat fluxes, water reservoir evo-  
21 lution, etc.). It uses DART model (Discrete Anisotropic  
22 Radiative Transfer) for simulating radiative mechanisms:  
23 3D radiative budget of 3D scenes and their remote sensing  
24 images expressed in terms of reflectance or brightness tem-  
25 perature values, for any atmosphere, wavelength, sun/view  
26 direction, altitude and spatial resolution. It uses an innova-  
27 tive multispectral approach (ray tracing, exact kernel, dis-  
28 crete ordinate techniques) over the whole optical domain.

29 This paper presents two major and recent improvements of  
30 DART for adapting it to urban canopies. (1) Simulation of  
31 the geometry and optical characteristics of urban elements  
32 (houses, etc.). (2) Modeling of thermal infrared emission by  
33 vegetation and urban elements. The new DART> version  
34 was used in the context of the CAPITOUL project. For that,  
35 districts of the Toulouse urban data base (Autocad format)  
36 were translated into DART scenes. This allowed us to  
37 simulate visible, near infrared and thermal infrared satellite  
38 images of Toulouse districts. Moreover, the 3D radiation  
39 budget was used by DARTEB for simulating the time evo-  
40 lution of a number of geophysical quantities of various sur-  
41 face elements (roads, walls, roofs). Results were successfully

compared with ground measurements of the CAPITOUL 42  
project. 43

### 1. Introduction 44

45 Modeling the radiative behavior and the energy  
46 budget of terrestrial surfaces is relevant for many  
47 scientific domains. It is typically the case for  
48 studying vegetation functioning with remotely  
49 acquired information. For example, the albedo  
50 of a canopy with an anisotropic Bidirectional  
51 Reflectance Factors (BRF) may be underesti-  
52 mated by as much as 45% if it is computed with  
53 nadir reflectance only (Kimes and Sellers 1985).  
54 Radiative transfer models have the potential for  
55 correcting this type of error. However, in order to  
56 be efficient tools, models must account for the  
57 three dimensional (3D) nature of Earth surfaces.  
58 Neglect of the 3D structure of canopies can lead  
59 to errors on the 3D radiation budget and remote  
60 sensing measurements. For example, it can  
61 lead to errors on vegetation BRF and direc-  
62 tional brightness temperature (DTDF) distribu-  
63 tion functions as large as 50%, depending on  
64 instrumental (e.g., view and sun directions) and  
65 experimental (e.g., vegetation heterogeneity) con-  
66 ditions (Gastellu-Etchegorry et al. 1999). The  
67 problem is similar for urban canopies due to their

---

Correspondence: Jean Philippe Gastellu-Etchegorry, Centre  
d'Etudes Spatiales de la BIOSphère Paul Sabatier University,  
CNES – CNRS, IRD 18 avenue Edouard Belin, BPi 2801, 31401  
Toulouse Cedex 4, France (E-mail: gastellu@cesbio.cnes.fr)

1 strong spatial heterogeneity. The application of  
 2 radiative transfer modeling to urban surfaces is  
 3 important in the context of the advent of satellite  
 4 sensors with spatial and spectral resolutions that  
 5 are more and more adapted to urban characteris-  
 6 tics such as building dimensions and temperature  
 7 spatial variability. It explains the numerous works  
 8 conducted in the field of remote sensing of urban  
 9 surfaces (Voogt and Oke 1998; Soux et al. 2004).  
 10 The use of descriptions with qualitatively based  
 11 land use data instead of more fundamental surface  
 12 descriptors is a source of inaccuracy for modeling  
 13 BRFs and DTDFs (Voogt and Oke 2003).

14 These remarks stress the usefulness of 3D ra-  
 15 diative transfer models. The DART (Discrete  
 16 Anisotropic Radiative Transfer) model (Gastellu-  
 17 Etchegorry et al. 1996) was developed in this  
 18 context for simulating remote sensing images  
 19 of 3D vegetation canopies in the visible/near in-  
 20 frared (NIR) spectral domain. However, it did  
 21 not model thermal infrared (TIR) emission and  
 22 could not operate with urban landscapes. After a  
 23 brief introduction of DART, this paper presents  
 24 two major and recent improvements that allow  
 25 DART to operate on urban landscapes, possibly  
 26 with vegetation, topography, atmosphere, and at-  
 27 mospheric turbidity within the scene, over the  
 28 whole optical domain. (1) Simulation of the geo-  
 29 metry and optical characteristics of urban elements  
 30 (houses, etc.). (2) Modeling of TIR emission by  
 31 vegetation and urban elements. As a result, the  
 32 present DART model simulates the radiation bud-  
 33 get and remote sensing images of natural and ur-  
 34 ban canopies, for any experimental (sun direction,  
 35 canopy heterogeneity, topography, more or less  
 36 turbid atmosphere, etc.) and instrumental (view  
 37 direction, spatial resolution, etc.) configuration.

38 The last part of the paper presents results ob-  
 39 tained in the context of the CAPITOU project,  
 40 thanks to the above mentioned improvements.  
 41 Firstly, visible, NIR and TIR satellite images of  
 42 Toulouse districts are shown. They were obtained  
 43 with DART scenes that were directly derived  
 44 from the Toulouse urban data base (Autocad for-  
 45 mat). Secondly, an extension of the DART mod-  
 46 el, called DARTEB (DART energy budget), that  
 47 is being developed for simulating the 3D energy  
 48 budget of vegetation and urban canopies is pres-  
 49 ented. Finally, preliminary results from DARTEB  
 50 are compared with ground measurements of the  
 51 CAPITOU project.

## 2. DART model

52

DART was originally developed for simulating  
 BRFs, remote sensing images and the spectral  
 radiation budget of 3D natural (e.g., trees, roads,  
 grass, soil, water) landscapes in the visible and  
 short wave infrared domains. Since its first re-  
 lease in 1996, it was successfully tested, in the  
 case of vegetation canopies, against reflectance  
 measurements (Gastellu-Etchegorry et al. 1999)  
 and against a number of 3-D reflectance models  
 (e.g., *Flight* (North 1996), *Sprint* (Thompson and  
 Goel 1998), *Raytran* (Govaerts and Verstraete  
 1998)), in the context of the RAMI (RADiation  
 transfer Model Intercomparison) experiment  
 (Pinty et al. 2001, 2004; Widlowski et al. 2007,  
 2008). Only BRFs could be compared because  
 DART is the only 3-D model that simulates  
 images.

DART was successfully used in many scientific  
 domains: impact of canopy structure on satellite  
 images texture (Pinel and Gastellu-Etchegorry  
 1998) and reflectance (Gastellu-Etchegorry et al.  
 1999), 3D distribution of photosynthesis and pri-  
 mary production rates of vegetation canopies  
 (Guillevic and Gastellu-Etchegorry 1999), in-  
 fluence of Norway forest spruce structure and  
 woody elements on LAI retrieval (Malenovský  
 et al. 2005) and canopy reflectance (Malenovský  
 et al. 2008), determination of a new hyperspectral  
 index for chlorophyll estimation of forest canopy  
 (Malenovský et al. 2006), etc.

DART simulates radiative transfer in heteroge-  
 neous 3-D landscapes with the exact kernel and  
 discrete ordinate methods. It uses an iterative ap-  
 proach: radiation intercepted in iteration “*i*” is  
 scattered in iteration “*i* + 1”. Any landscape is  
 simulated as a rectangular matrix of parallelepi-  
 pedic cells. Figure 1 illustrates the way urban and  
 natural landscapes are simulated, possibly with  
 topography and atmosphere. The atmosphere is  
 made of cells the size of which increases with  
 altitude. Radiation is restricted to propagate in  
 a finite number of directions ( $\Omega_i$ ) with an angular  
 sector width ( $\Delta\Omega_i$ ) (sr). Any set of  $N$  discrete  
 directions can be selected ( $\sum_{n=1}^N \Delta\Omega_n = 4\pi$ ).  
 A radiation that propagates along direction ( $\Omega_i$ )  
 at a position  $r$  is called a source vector  $W(r, \Omega_i)$ .  
 It has 3 components: total radiation  $W$ , radiation  
 unrelated to leaf mesophyll and polarization de-  
 gree associated to first order scattering.

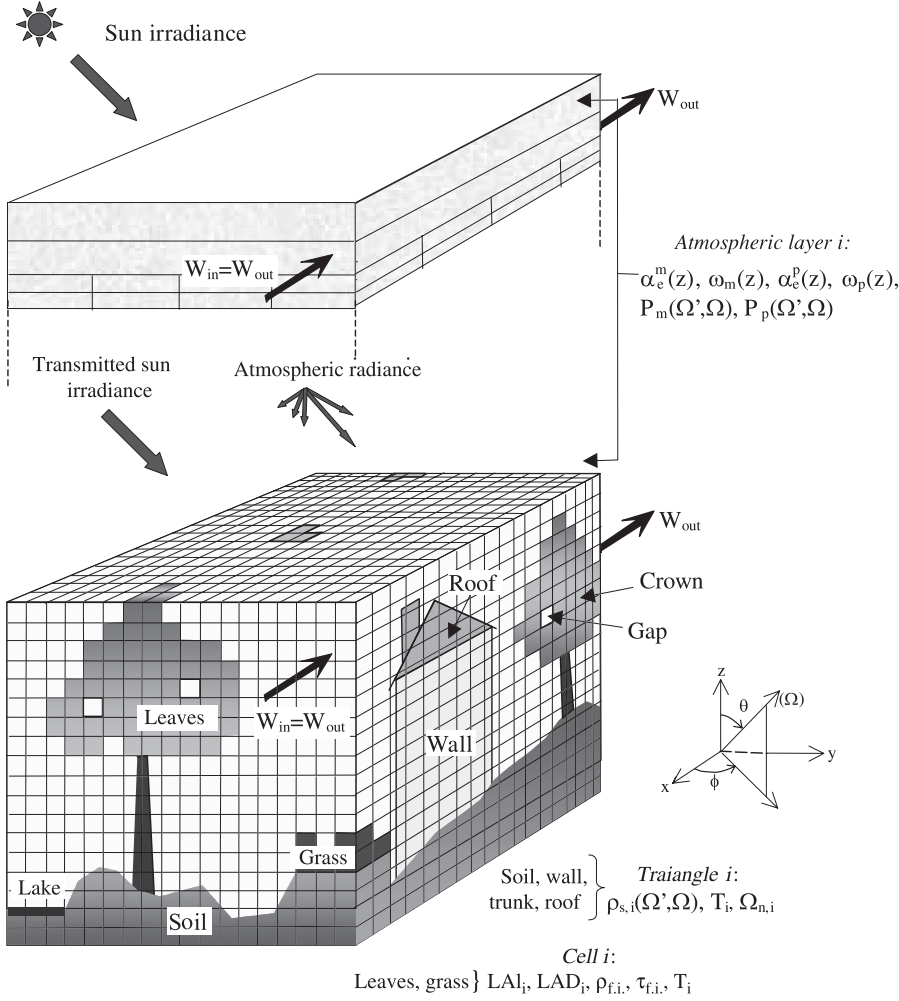


**Fig. 1.** “Atmosphere + Earth” simulation used as an input to DART model. It shows a mixed “built-up/natural Earth landscape + atmosphere”

1 The number of possible ray paths is finite be-  
 2 cause the number of directions is finite and be-  
 3 cause within each DART cell, the origin of any  
 4 ray is a point  $P$  among the  $N_{sc}^3$  points that sample  
 5 the cell or the  $6 \cdot N_{sf}^2$  points that sample the 6 cell  
 6 faces. Thus, there are  $(N_{sc}^3 + 6 \cdot N_{sf}^2)$  paths for  
 7 each discrete direction, with  $N_{sf} = N_{sc}$  for scatter-  
 8 ing mechanisms, and  $N_{sf} = 2 \cdot N_{sc}$  for emission  
 9 mechanisms, usually with  $N_{sc} = 7$ . In a first step,  
 10 DART computes the  $(N_{sc}^3 + 6 \cdot N_{sf}^2)$  possible  
 11 paths from cell  $(0, 0, 0)$ . This pre-computation  
 12 eliminates unnecessary repetitive computations  
 13 during the tracking of source vectors because it  
 14 allows a simple calculation of any ray path from  
 15 any cell: the coordinates of the  $i$ th cell encoun-  
 16 tered by a source vector that propagates within  
 17 the scene are the coordinates of the cell where it  
 18 originates plus the  $i$ th coordinates of the pre-  
 19 computed ray path that has the same direction.

20 Scene irradiance has 2 components: direct sun  
 21  $W(\Omega_s)$  and atmospheric  $W_a(\Omega_n)$  source vectors.

$W(\Omega_s)$  propagates along direction  $(\Omega_s)$ .  $W(\Omega_s)$  22  
 and  $W_a(\Omega_n)$  are simulated from a fictitious cell 23  
 layer on top of the scene (Fig. 1), with values 24  
 equal to: 25

$$W(\Omega_s) = E_s(\Omega_s) \cdot |\mu_s| \cdot \Delta x \cdot \Delta y$$

$$W_a(\Omega_n) = L_a(\Omega_n) \cdot |\mu_n| \cdot \Delta x \cdot \Delta y \cdot \Delta \Omega_n$$

where  $\Delta x \cdot \Delta y$  is the area of the cell face,  $\mu_s =$  27  
 $\cos \theta_s$ ,  $\mu_n = \cos \theta_n$ ,  $E_s(\Omega_s)$  is the solar con- 28  
 stant at the top of the scene, and  $\Omega_s$  denotes 29  
 the solar incident direction.  $L_a(\Omega_n)$  is the atmo- 30  
 spheric radiance along direction  $(\Omega_n)$ , with 31  
 $n \in [1 N']$ , where  $N'$  is the number of downward 32  
 discrete directions. It is null at the top of the 33  
 atmosphere. 34

Generally speaking, two types of radiation in- 35  
 teraction take place. (1) Volume interaction with- 36  
 in turbid cells the juxtaposition of which is used 37  
 to simulate vegetation elements. (2) Surface in- 38  
 teraction on triangles the juxtaposition of which 39  
 is used to simulate urban surfaces and topogra- 40

1 phy. Radiation interaction within turbid cells is  
 2 described in Gastellu-Etchegorry et al. (2004).  
 3 Within cell first order scattering is exactly com-  
 4 puted. As expected, simplifying hypotheses are  
 5 used for simulating multiple scattering. It is  
 6 now computed with a much faster approach  
 7 than the initial “harmonic expansion approach:  
 8 it is computed using the energy intercepted with-  
 9 in a finite number of incident angular sectors  
 10  $\Omega_{\text{sect},k}$  that sample the  $4\pi$  space of directions  
 11 ( $\sum \Omega_{\text{sect},k} = 4\pi$ ). The number of sectors can be  
 12 as large as the number of directions of ray prop-  
 13 agation, but a number equal to 6 leads to very  
 14 accurate results, with relative errors smaller than  
 15  $10^{-3}$  (Gastellu-Etchegorry et al. 2004). Another  
 16 major improvement concerns scattering by turbid  
 17 cells. Now, scattered radiation starts from a point  
 18  $M_s(z_{m\uparrow})$  for upward directions ( $\Omega_v$ ) and a point  
 19  $M_s(z_{m\downarrow})$  for downward directions ( $\Omega_v$ ). The alti-  
 20 tudes  $z_{m\uparrow}$  and  $z_{m\downarrow}$  are those that give exact results  
 21 for two specific upward  $\Omega_{m\uparrow}$  and downward  $\Omega_{m\downarrow}$   
 22 directions in the case of homogeneous turbid me-  
 23 dia. Optimal values are  $\theta_{m\uparrow} = 20^\circ$  and  $\theta_{m\downarrow} = 160^\circ$ .  
 24 These points are computed for each cell face  
 25  $f (f \in [1, 6])$  that intercepts incident rays, and for  
 26 each angular sector “incident” on the cell face  
 27 (Martin 2006). This implies that intercepted vec-  
 28 tor sources  $W_{\text{int}}(f, \Omega_{\text{sect},k})$  are stored per cell face  
 29  $f$  and per incident angular sector  $\Omega_{\text{sect},k}$ .

30 Thus:

$$W_{\text{int}}(f, \Omega_{\text{sect},k}) = \sum_{\Omega_s} W_{\text{int}}(f, \Omega_s),$$

32 with directions ( $\Omega_s$ ) within ( $\Omega_{\text{sect},k}$ ). For the case  
 33 “direct sun illumination”, there is only 1 sector.

34 Atmospheric radiative transfer modeling is im-  
 35 plemented for any spectral band in the optical  
 36 domain from the ultraviolet up to the thermal  
 37 infrared (Dallest 2001; Gascon 2001). It simu-  
 38 lates the atmospheric backscattering phenome-  
 39 non, which avoids the need to couple DART  
 40 with an atmospheric model. Atmospheric optical  
 41 properties are characterized by the molecular  
 42  $P_m(\lambda, \Omega', \Omega)$  and aerosol  $P_p(\lambda, \Omega', \Omega)$  phase func-  
 43 tions and by a number of profiles (molecular ex-  
 44 tinction coefficient  $\alpha_e^m(\lambda, z)$  and spherical albedo  
 45  $\omega_m(\lambda, z)$ , aerosol extinction coefficient  $\alpha_e^p(\lambda, z)$   
 46 and spherical albedo  $\omega_p(\lambda, z)$ ). These quantities  
 47 are specified by the operator or come from a data  
 48 base ( $[0.3 \mu\text{m} - 30 \mu\text{m}]$ ) pre-computed with the  
 49 Modtran atmospheric model (Berk et al. 1989),  
 50 for a few predefined atmospheres. DART atmo-

spheric reflectance, transmittance and brightness  
 temperature are very close to Modtran simula-  
 tions in the case of lambertian horizontal Earth  
 surfaces (Grau 2008).

Images are simulated in the focal plane of the  
 satellite sensor (Gentine 2002) with the steps:

- Projection of upward source vectors onto an  
 oversampled horizontal grid on top the scene  
 simulation. The cross section of the emitters  
 and scatterers at the origin of the signal is  
 used for improving the geometric accuracy of  
 images, especially for scenes with marked 3D  
 architectures (urban elements, topography).
- Bi-linear interpolation method that projects  
 the horizontal upper grid of the scene onto  
 an over sampled grid in the sensor plane, at  
 any altitude (bottom to top of the atmosphere).
- Signal convolution with sensor spectral  
 characteristics.

DART works with a specifically designed  
 Graphic User Interface (GUI) for imputing para-  
 meters that characterize the landscape and the  
 view and illumination conditions.

### 3. Simulation of urban elements

Urban elements (e.g., roads, wall, roof) are sim-  
 ulated as the juxtaposition of parallelograms  
 and triangles, hereafter called “opaque figures”.  
 Opaque figures are also used for simulating to-  
 pography. As a result, DART cells can be empty  
 or filled with either turbid media or plane sur-  
 faces. Although all opaque figures undergo the  
 same radiative mechanisms, cells that contain  
 opaque figures (Fig. 2) belong to different cell  
 types (e.g., roof and wall cells) for differentiating  
 their radiation budget. This is used also for  
 obtaining realistic scene displays. The type of a  
 cell that contains all or part of an opaque figure is  
 the type of that opaque figure. Figure 2 shows the

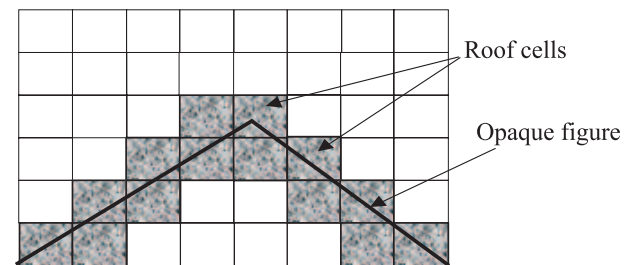
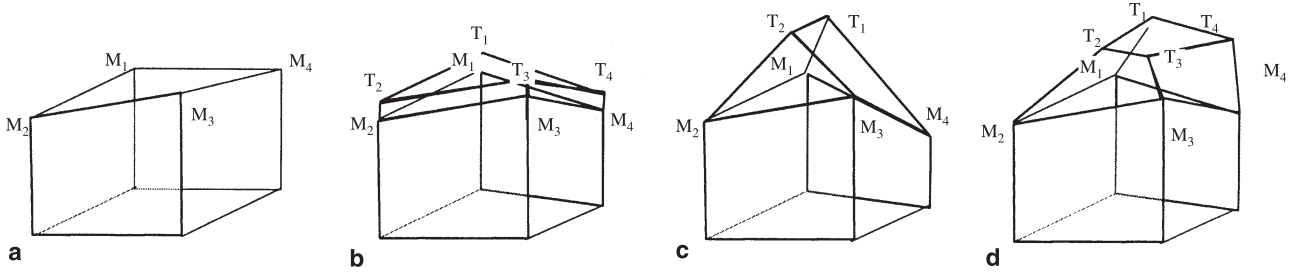


Fig. 2. Cells “Roof” and opaque figures



**Fig. 3.** The 4 pre-defined house types. (a) No roof. (b) Plate. (c) Classic. (d) Complex

- 1 intersection of cells with 2 opaque figures that  
 2 simulate a roof. These cells are called *Roof cells*.  
 3 Actually, cells can contain or be intersected by  
 4 several figures. The type of a cell crossed by  
 5 figures that belong to different urban elements  
 6 (e.g., roof + wall) is the type of the last simulated  
 7 urban element.  
 8 From the radiative transfer point of view,  
 9 buildings can have very complex shapes. They  
 10 are the superimposition of generic volume ele-  
 11 ments (e.g., tetrahedron, pyramid, column, chim-  
 12 ney, etc) defined by any 8 points and 6 faces.  
 13 Urban canopy simulation is eased with the pre-  
 14 definition of four major urban elements:
- 15 • *Small wall*: it is defined by its 4 upper corners  
 16 and its optical properties.
  - 17 • *House*: it is made of 2 elements (4 walls + 1  
 18 roof) simulated by a generic model.
    - 19 – The 4 walls are defined by their optical  
 20 properties and their 4 upper corners ( $x, y, z$ ).
    - 21 – The roof. Its 4 lower points are the 4 upper  
 22 corners of the walls, whereas its top is de-  
 23 fined by 0 to 4 points, depending on the type  
 24 of roof (Fig. 3).
  - 25 \* No roof. The roof is made of 2 triangles  
 that link the top corners of the walls  
 (Fig. 3a).
  - \* Plate. The roof is a layer defined by a verti-  
 cal shift (roof depth) from the 4 top wall  
 corners ( $x, y, z$ ), which defines the 4 points  
 $T_1, T_2, T_3$  and  $T_4$  of the roof (Fig. 3b).
  - \* Classic. The roof is defined by the 2 up-  
 per points  $T_1, T_2$  of the roof (Fig. 3c).
  - \* Complex. The roof is defined by the 4  
 upper points  $T_1, T_2$  of the roof (Fig. 3d).
- 36 • *Building*: set of houses with identical optical  
 properties for their walls and roofs.
  - 37 • *Road*: defined by its width and the coordinates  
 38 ( $x, y$ ) of the projection of consecutive points

onto a horizontal plane. The associated seg- 40  
 ments define the cells called *Route*. 41

Any radiation scattered  $W_{\text{scat}}(\Omega_v)$  by an opa- 42  
 que surface of reflectance  $\rho(\Omega_s, \Omega_v)$  is the prod- 43  
 uct of the incident vector source  $W_{\text{in}}(\Omega_s)$  by 44  
 the transfer function  $T(\Omega_s, \Omega_v)$ , which depends 45  
 on  $\rho(\Omega_s, \Omega_v)$ . There are 4 possible types of 46  
 reflectance: 47

- *Type 0*: “Lambertian + random spatial vari- 48  
 ability”. 49
- *Type 1*: “Lambertian + specular reflectance 50  
 $\rho_{\text{spec}}(\Omega_s, \Omega_v)$ ”. 51
- *Type 2*: “Hapke + specular”. 52
- *Type 3*: Pre-computed functions  $T_d(\Omega_s, \Omega_v)$ , 53  
 $T_{\text{spe}}(\Omega_s, \Omega_v)$  and  $T_{\text{pol}}(\Omega_s, \Omega_v)$  54

These 4 types of reflectance and the associated 55  
 physical laws are presented in the Annex. 56

Vegetation elements are simulated as the jux- 57  
 taposition of turbid cells. These cells contain a 58  
 turbid medium made of infinitesimal planar ele- 59  
 ments that are characterized by specific optical 60  
 properties (reflectance, transmittance), a statisti- 61  
 cal distribution of orientations (LAD: Leaf Angle 62  
 Distribution) and a surface density (LAI: Leaf 63  
 Area Index). 64

#### 4. Ray tracking in presence of opaque figures 65

Surface scattering and emission mechanisms as- 66  
 sociated with urban elements are modeled using 67  
 surface optical properties introduced in the pre- 68  
 vious chapter. The radiation scattered and/or 69  
 emitted by opaque figures can be intercepted by 70  
 other scene elements (i.e., turbid medium or opa- 71  
 que element) within the cell itself and/or other 72  
 cells (Gastellu-Etchegorry 2007). Approaches 73  
 adopted for managing ray interception by opaque 74  
 figures, for determining the origins of rays that 75  
 are scattered and emitted by opaque figures, and 76

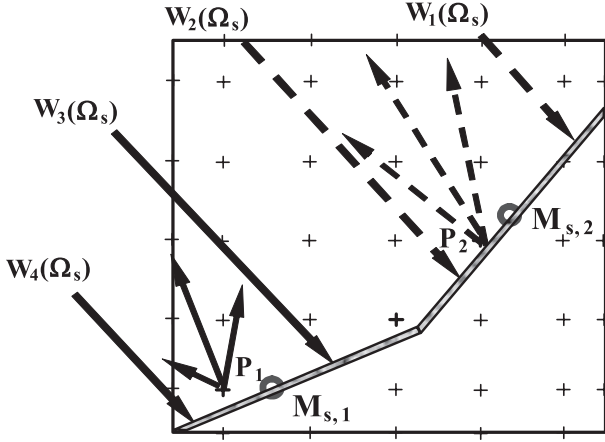


**Fig. 4.** Interception of 4 rays by 2 figures.  $W_1$  and  $W_2$  are intercepted by Fig. 2.  $W_3$  and  $W_4$  are intercepted by Fig. 1. Resulting effective points of emission are  $P_2$  and  $P_1$

- 1 for tracking rays in presence of opaque figures
- 2 are presented below.

#### 3 4.1 Radiation interception by an opaque figure

4 The within cell interaction “ray – figures (i.e.,  
5 triangle/parallelogram)” is modeled in 2 steps:

6 1) Determination if the ray (i.e.,  $W_1(\Omega_s)$ ,  
7  $W_2(\Omega_s)$ ,  $W_3(\Omega_s)$ ,  $W_4(\Omega_s)$  in Fig. 4) incident  
8 on the cell intercepts the plane {point, normal  
9 vector} that contains every figure in the cell.

10 2) If there is a point of interception ( $M$ ), it is  
11 checked if this point is both in the cell and  
12 in the figure. A test on the co-ordinates of ( $M$ )  
13 indicates if this point belongs or not to the  
14 cell. Two steps allow one to determine if  
15 ( $M$ ) belongs to the figure:

- 16 (i) Change of reference to express the co-ordi-  
nates of  $M$  in the reference of the figure.
- 17 (ii) These co-ordinates are submitted to  $N$   
inequations, associated to  $N$  constraints,  
18  $N$  being the number of edges of the figure.

#### 21 4.2 Origin of radiation scattered/emitted 22 by an opaque figure

23 Rays are scattered and emitted from  $(N_{sc}^3 +$   
24  $6 \cdot N_{sf}^2)$  predefined points. The determination of  
25 these points is carried out in 2 stages:

- 26 1) For each intercepting figure, a barycentric  
27 method computes the exact emission point:  
28 if a ray intersects a figure in a cell, the new

exact emission point of the figure is the ener- 29  
gy barycentre of this intersection point and 30  
the exact emission point, calculated before 31  
this intersection (e.g.,  $M_{s,1}$  and  $M_{s,2}$  in Fig. 32  
4). This point is always on the figure. 33

- 2) Determination of the effective point of emis- 34  
sion (e.g.,  $P_1$  and  $P_2$  in Fig. 4) among the 35  
 $(N_{sc}^3 + 6 \cdot N_{sf}^2)$  points which sample the cell. 36  
The center (called “sub-center”) of the sub- 37  
cell that contains ( $M_{si}$ ) is the first guess. It is 38  
determined by thresholding the co-ordinates 39  
of ( $M_{si}$ ). If it is not acceptable, another point 40  
is searched for. In order to be accepted, a 41  
point  $P_i$  must be as close as possible of 42  
( $M_{si}$ ) and must verify: 43

- a) ( $P_i$ ) is outside the volume bounded by the 44  
emitting figure. 45
- b) there is no figure between ( $P_i$ ) and ( $M_{si}$ ). 46

The search of the effective point  $P_i$  uses a 47  
test on the directions of vectors “sub-center → 48  
figure” and “perpendicular of the figure”. If 49  
these directions are: 50

- not opposed (i.e., cosine  $< 0$ ), with no figure 51  
between ( $M_{si}$ ) and ( $P_i$ ): ( $P_i$ ) is accepted. 52
- opposite: ( $P_i$ ) is shifted with a sub-grid shift 53  
( $\pm \Delta X/N$ ,  $\pm \Delta Y/N$  or  $\pm \Delta Z/N$ ) along the axis 54  
( $Ox$ ,  $Oy$  or  $Oz$ ) for which the absolute value of 55  
the component in  $X$ ,  $Y$  or  $Z$  of the normal vec- 56  
tor to the figure is largest.  $\Delta X$ ,  $\Delta Y$ ,  $\Delta Z$  are the 57  
cell dimensions. 58

If no point ( $P_i$ ) is found both within the cell 59  
and outside the scene element bounded by the 60  
figure, ( $P_i$ ) is searched in a systematic way 61  
among all possible  $(N_{sc}^3 + 6 \cdot N_{sf}^2)$  points ( $P_i$ ) of 62  
the cell, starting from closer centers. If no point 63  
is found, energy is lost and stored in a variable. 64  
Actually, this energy loss is always negligible. 65

#### 4.3 Ray tracking from an opaque figure 66

The interest of effective points of emission ( $P_i$ ) 67  
is that all possible paths that start from them are 68  
pre-calculated. The actual path of any ray that 69  
comes from a point ( $P_i$ ) of the cell is pre-cal- 70  
culated as far as the intersection point ( $Q$ ) of the ray 71  
with the horizontal plane that contains the upper 72  
or bottom face of the cell. Then, the ray follows 73  
the pre-calculated path which originates in the 74  
closer sub-center ( $E_i$ ) of the horizontal plane. 75

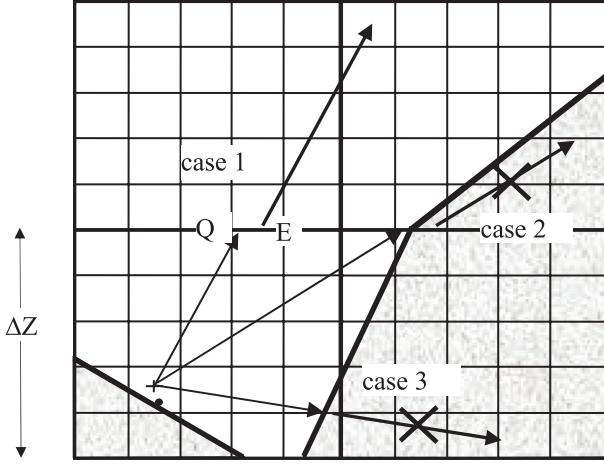


**Fig. 5.** Illustration of ray tracking in presence of opaque figures

- 1 Figure 5 illustrates some cases that occur during  
 2 ray tracking in presence of opaque figures.
- 3 • *Case 1:* Occurrence of a small geometrical  
 4 shift between the points ( $Q_i$ ) and ( $E_i$ ).
- 5 • *Case 2:* The ray goes under the figure in the  
 6 following cell. If the segment ( $Q_i E_i$ ) intersects  
 7 a figure, the energy of the ray is stored on the  
 8 first intersected figure.
- 9 • *Case 3:* The ray intersects a figure in the cell.  
 10 If the segment ( $Q_i E_i$ ) intersects a figure of the  
 11 cell, the energy of the ray is attributed to the  
 12 closest intercepted figure.

## 13 5. Modeling emission mechanisms

14 TIR modeling was introduced by Boyat (2001)  
 15 and Guillevic et al. (2003) with methods (i.e.,

discrete ordinate and exact kernel methods, 16  
 etc.) similar to those used for tracking visible 17  
 and NIR radiation. Major recent improvements 18  
 are presented below. 19

### 5.1 Thermal emission of leaf turbid cells 20

Compared to radiative transfer modeling in the 21  
 short wavelengths, a major specificity of TIR 22  
 modeling is the emission of turbid leaf cells. In- 23  
 deed, it is calculated on a cell per cell basis as the 24  
 integration of the Planck law over a specified 25  
 spectral band. 26

#### • Theoretical approach 27

Let us consider the radiation  $dW_{ij}(\lambda, \Omega_v, T)$  28  
 that a cell emits along direction  $\Omega_v$ , through 29  
 a surface element  $S_{ij}$  of face  $k$  of the cell 30  
 (Fig. 6). The emission comes from the cell vol- 31  
 ume  $V(k, \Omega_v)$ . 32

We have: 33

$$dW_{ij}(\lambda, \Omega_v, T) = L_{B,f}(\lambda, T) \cdot G(\Omega_v) \cdot u_f \cdot \Delta\Omega_v \cdot \int_{V(k, \Omega_v)} \exp[-G(\Omega_v) \cdot u_f \cdot \Delta l(dV)] \cdot dV$$

$$dW_{ij}(\lambda, \Omega_v, T) = L_{B,f}(\lambda, T) \cdot \cos(\Psi_{nv}) \cdot \Delta\Omega_v \cdot \{1 - \exp[-G(\Omega_v) \cdot u_f \cdot L_{ij}]\} \cdot S_{ij}$$

$L_{B,f}(\lambda, T) = \epsilon_{f,t} \cdot L_B(\lambda, T)$ : radiance of a leaf 35  
 with temperature  $T$ , at wavelength  $\lambda$ . 36

$\Psi_{nv}$ : angle between direction  $\Omega_v$  and the normal 37  
 $\Omega_n$  of the face. 38

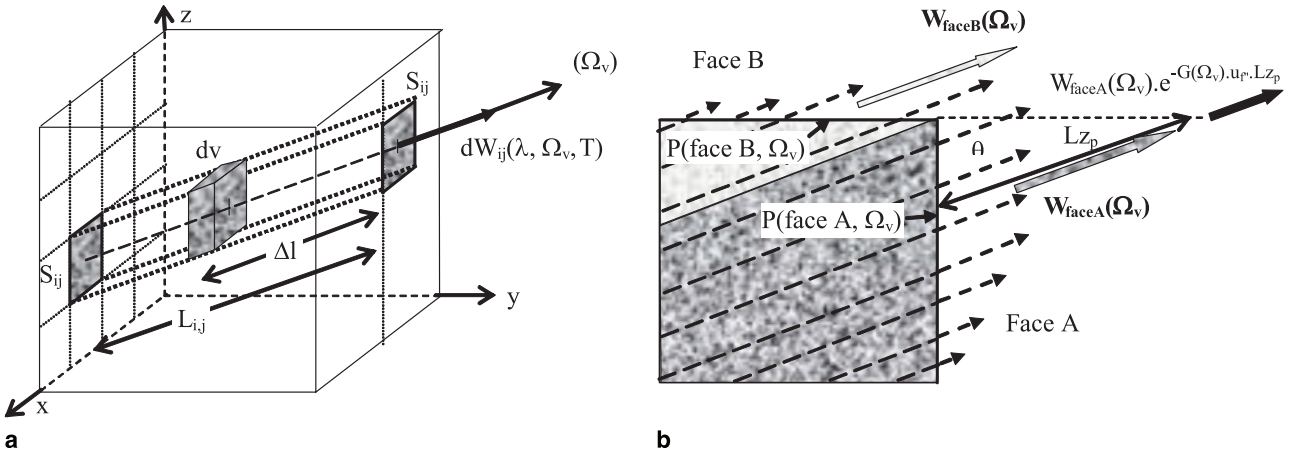


**Fig. 6.** Computation of the TIR emission of a turbid cell ( $T, u_f, \text{LAD}$ )



1 Thus, the total emitted energy that crosses face  
2  $k$  is:

$$\begin{aligned} W_{1 \text{ face } k}(\Omega_v) &= \sum_{ij} dW_{ij}(\Omega_v) \\ &= L_{B,f}(\lambda, T) \cdot \cos(\Psi_{nv}) \cdot \Delta\Omega_v \\ &\quad \cdot \sum_{ij} \{1 - \exp[-G(\Omega_v) \cdot u_f \cdot L_{ij}]\} \cdot S_{ij} \end{aligned}$$

4 If there are  $\mathcal{T}$  leaf species ( $u_{f,t}, T_t, G_t(\Omega_v)$ ), with  
5  $t \in [1 \mathcal{T}]$ , the total emission through face  $k$  is:

$$\begin{aligned} W_{1 \text{ face } k}(\Omega_v) &= \frac{\sum_t L_{B,f}(\lambda, T_t) \cdot G_t(\Omega_v) \cdot u_{f,t} \cdot \cos(\Psi_{nv}) \cdot \Delta\Omega_v}{\sum_t G_t(\Omega_v) \cdot u_{f,t}} \\ &\quad \cdot \sum_{ij} \left\{ 1 - \exp \left[ - \sum_t G_t(\Omega_v) \cdot u_{f,t} \cdot L_{ij} \right] \right\} \cdot S_{ij} \end{aligned}$$

7 Source vector  $dW_{ij}(\lambda, \Omega_v, T)$  that escapes sur-  
8 face  $S_{ij}$  along direction ( $\Omega_v$ ) is the sum of the  
9 energy emitted by all volume elements  $dv$  within  
10 volume  $S_{ij} \times L_{ij}$ . Total energy emitted along ( $\Omega_v$ )  
11 comes from 1 up to 3 cell faces depending on ( $\Omega_v$ ).

### 12 • Within cell scattering

13 Part of the TIR emission is intercepted before  
14 exiting the cell, which leads to scattering of order  
15 1 and larger.

16 Thus, the energy intercepted along the direc-  
17 tion ( $\Omega_v$ ) is:

$$\begin{aligned} W_{\text{int}}(\lambda, \Omega_v, T) &= L_{B,f}(\lambda, T) \cdot G(\Omega_v) \cdot u_f \cdot \Delta\Omega_v \\ &\quad \cdot \left\{ V_{\text{cell}} - \frac{\cos \Psi_{nv}}{G(\Omega_v) \cdot u_f} \right. \\ &\quad \left. \cdot \sum_k \sum_{ij} [1 - e^{-G(\Omega_v) \cdot u_f \cdot L_{ij}}] \cdot S_{ij} \right\} \end{aligned}$$

19 With  $\mathcal{T}$  leaf species ( $u_{f,t}, T_t, G_t(\Omega_v)$ ) and  $t \in$   
20  $[1 \mathcal{T}]$ , total energy intercepted along ( $\Omega_v$ ) is:

$$\begin{aligned} W_{\text{int}}(\lambda, \Omega_v, T) &= \sum_t L_{B,f}(\lambda, T_t) \cdot G_t(\Omega_v) \cdot u_{f,t} \cdot \Delta\Omega_v \\ &\quad \cdot \left\{ V_{\text{cell}} - \frac{\cos \Psi_{nv}}{\sum_t G_t(\Omega_v) \cdot u_{f,t}} \right. \\ &\quad \left. \cdot \sum_k \sum_{ij} [1 - e^{-\sum_t G_t(\Omega_v) \cdot u_{f,t} \cdot L_{ij}}] \cdot S_{ij} \right\} \end{aligned}$$

22 Total interception is:

$$W_{\text{int}}(\lambda, T) = \sum_{v=1}^{N_{\text{dir}}} W_{\text{int}}(\lambda, \Omega_v, T)$$

Scattering radiation that exits the cell is simu- 24  
lated as a geometric series: 25

$$\begin{aligned} W_M(\lambda, T) &= W_{\text{int}}(\lambda, T) \cdot \{ \omega_\lambda \cdot \langle T \rangle \\ &\quad + \omega_\lambda \cdot \langle T \rangle \cdot [\omega_\lambda - \omega_\lambda \cdot \langle T \rangle] \\ &\quad + \omega_\lambda \cdot \langle T \rangle \cdot [\omega_\lambda - \omega_\lambda \cdot \langle T \rangle]^2 + \dots \} \\ W_M(\lambda, T) &= \left[ \frac{\omega_\lambda \cdot \langle T \rangle}{1 - \omega_\lambda \cdot [1 - \langle T \rangle]} \right] \cdot W_{\text{int}}(\lambda, T) \end{aligned}$$

with  $\langle T \rangle$  = mean transmittance on all  $N_{\text{dir}}$  direc- 27  
tions from cell center: 28

$$\langle T \rangle = \frac{1}{4\pi} \cdot \int_{4\pi} e^{-G(\Omega) \cdot u_f \cdot \Delta m(\Omega)} \cdot d\Omega$$

where  $\Delta m(\Omega_v)$  = path along ( $\Omega_v$ ) from the cell 30  
center to the exit cell face. 31

With  $\mathcal{T}$  leaf species 32

$$\begin{aligned} (u_{f,t}, T_t, G_t(\Omega_v)): \omega &= \frac{\sum_t \omega_{f,t} \cdot u_{f,t}}{\sum_t u_{f,t}}, \quad \langle T \rangle = \Pi_t \langle T \rangle_t, \\ G(\Omega_v) \cdot u_f &= \sum_t G_t(\Omega_v) \cdot u_{f,t} \end{aligned}$$

The angular distribution of scattering is: 34

$$W_M(\lambda, \Omega_v, T) = W_M(\lambda, T) \cdot \frac{TG(\Omega_v) \cdot \Delta\Omega_v}{\sum_{v=1}^{N_{\text{dir}}} TG(\Omega_v) \cdot \Delta\Omega_v}$$

with 36

$$\begin{aligned} TG(\Omega_v) &= \sum_{i=1}^{N_{\text{dir}}} T_{\text{diff}}(\Omega_i, \Omega_v) \cdot G(\Omega_i) \cdot \Delta\Omega_i, T_{\text{diff}}(\Omega_i, \Omega_v) \\ &= \int_{\Delta\Omega_v} \frac{\int_{2\pi} \frac{g_f(\Omega_f)}{2\pi} \cdot |\Omega_i \cdot \Omega_f| \cdot f_d(\Omega_f, \Omega_s \rightarrow \Omega_v) \cdot d\Omega_f}{G(\Omega_s)} \\ &\quad \cdot d\Omega_v \end{aligned}$$

With  $\mathcal{T}$  leaf species: 38

$$\begin{aligned} TG(\Omega_v) &= \frac{\sum_t TG_t(\Omega_v) \cdot u_{f,t}}{\sum_t u_{f,t}} \Rightarrow W_M(\lambda, \Omega_v, T) \\ &= W_M(\lambda, T) \\ &\quad \cdot \frac{\sum_t TG_t(\Omega_v) \cdot u_{f,t} \cdot \Delta\Omega_v}{\sum_{v=1}^{N_{\text{dir}}} \sum_t TG_t(\Omega_v) \cdot u_{f,t} \cdot \Delta\Omega_v} \end{aligned}$$

The number of faces seen along  $\Omega_v$  is  $K \leq 3$ : 40

$$W_M(\lambda, \Omega_v, T) = \sum_{k=1}^K W_{M \text{ face } k}(\lambda, \Omega_v, T, k)$$

1 with  $W_{M \text{ face } k} \approx$  proportional to leaf area cross  
2 section:

$$S_{\text{eff}}(u_f, \text{LAD}, \Omega_v, k) = \frac{W_{1 \text{ face } k}(\lambda, \Omega_v, T)}{L_B(\lambda, \Omega_v, T)}$$

4 Thus:

$$W_{M \text{ face } k}(\lambda, \Omega_v, T) = \frac{W_{1 \text{ face } k}(\lambda, \Omega_v, T)}{\sum_{v=1}^K W_{1 \text{ face } k}(\lambda, \Omega_v, T)} \cdot W_M(\lambda, \Omega_v, T)$$

6 Total energy that exits face  $k$  along  $(\Omega_v)$ :

$$\begin{aligned} W_{\text{face } k}(\lambda, \Omega_v, T) &= W_{1 \text{ face } k}(\lambda, \Omega_v, T) \\ &\quad + W_{M \text{ face } k}(\lambda, \Omega_v, T) \\ &\Rightarrow W_{\text{face } k}(\lambda, \Omega_v, T) \\ &= L_B(\lambda, T) \cdot H_f(u_f, \text{LAD}, \Omega_v, k) \end{aligned}$$

8 where LAD

$$\begin{aligned} H_f(u_f, \text{LAD}, \Omega_v, k) &= S_{\text{eff}}(u_f, \text{LAD}, \Omega_v, k) \cdot \Delta\Omega_v \\ &\cdot \left[ 1 + \frac{S_{\text{eff}}(u_f, \text{LAD}, \Omega_v, k)}{\sum_{v=1}^K S_{\text{eff}}(u_f, \text{LAD}, \Omega_v, k)} \right. \\ &\quad \cdot \frac{TG(\Omega_v) \cdot \Delta\Omega_v}{\sum_{v=1}^{N_{\text{dir}}} TG(\Omega_v) \cdot \Delta\Omega_{rv}} \cdot \frac{\omega_\lambda \cdot \langle T \rangle}{1 - \omega_\lambda \cdot [1 - \langle T \rangle]} \\ &\quad \left. \cdot G(\Omega_v) \cdot u_f \cdot \int_{V_{\text{cell}}} (1 - e^{-G(\Omega_v) \cdot u_f \cdot \Delta l(dv)}) \cdot dv \right] \end{aligned}$$

In order to limit computer time,  $H_f(u_f, \text{LAD}, \Omega_v, k)$  is pre-computed for:

- all exact  $H_f(u_f, \text{LAD}, \Omega_v, k)$  values, if for each leaf species the number of  $u_f$  values is  $\leq 10$ .
- 10  $H_f(u_f, \text{LAD}, \Omega_v, k)$  values, if there is at least one leaf species for which the number of  $u_f$  values is  $> 10$ . Pre-computation is performed on 10 equidistant  $u_f$  values from  $u_{f, \text{min}}$  in to  $u_{f, \text{max}}$  for each leaf species. In a 2nd step, the exact  $H_f(u_f, \text{LAD}, \Omega_v, k)$  values are computed with a linear interpolation on the  $u_f$  values.

The precision of  $W(\lambda, \Omega_v, T, k)$  depends on the  $H_f$  precision and thus on the discretization level of the sub-faces  $S_{ij}$  used to calculate leaf cell emission  $W_1$  and scattering  $W_M$ . The estimate of  $W(\lambda, \Omega_v, T, k)$  is all the more precise as this discretization is fine; i.e., large number  $I \times J$  of sub-faces  $S_{ij}$ . Tests conducted with variable values of  $I$  and  $J$  showed that the pre-defined number  $I \times J$  ( $50 \times 50$ ) lead to errors systematically lower than 0.01 K.

Figure 7 shows DART simulated directional brightness temperature  $T_B(\Omega_v)$ , as a function of view zenith angle  $\theta_v$ , for a vegetation turbid medium (LAI=5), with 298 K leaf and soil temperature. It illustrates the impact of (1) the number

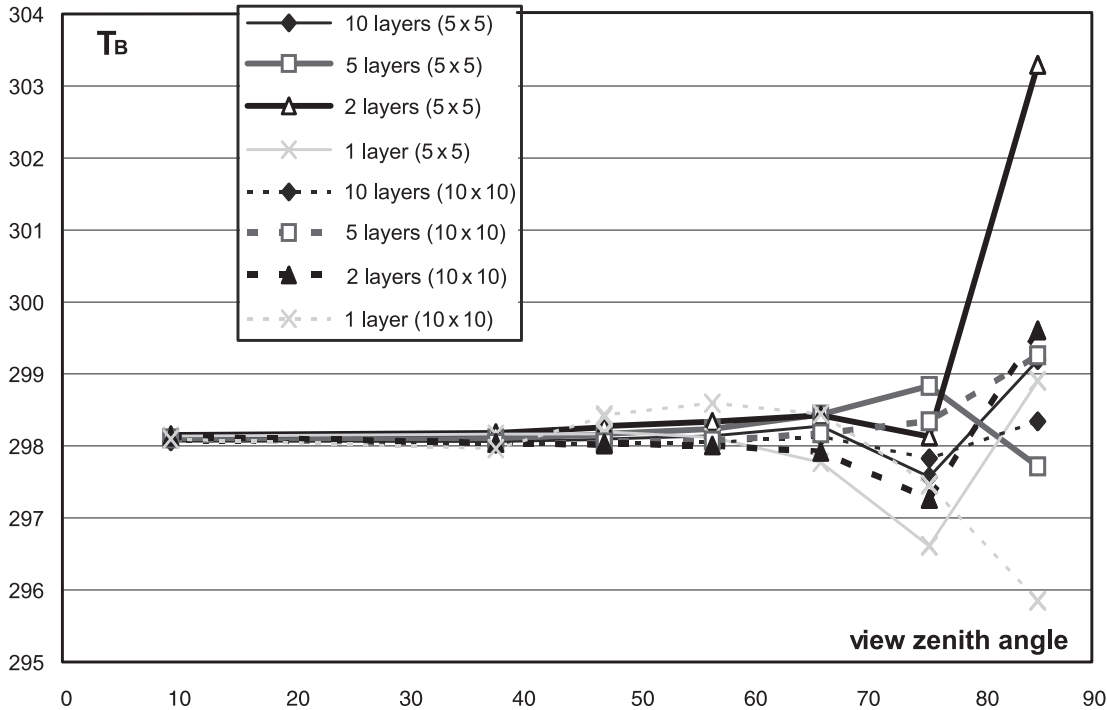


**Fig. 7.** Precision of  $T_{\text{app}}(\Omega_v)$  according to the view zenith angle, the discretization  $N_{sf}$  ( $5 \times 5$  or  $10 \times 10$ ) and the numbers of layers (1–10). LAI=5.  $T_f = 298$  K

1 of  $I \times J$  ( $5 \times 5$  and  $10 \times 10$ ) sub faces used for  
 2 computing the emission per cell face, and (2) the  
 3 number of layers (1, 2, 5 and 10) used to simulate  
 4 the turbid layer. Brightness temperature should  
 5 be 298 K for any direction. As expected, errors  
 6 decrease with the increase of the  $I \times J$  value and  
 7 the number of layers.

### 8 • Account of neighbor cells

9 Usually, the origin of any emitted ray  $W_{\text{face } k}$   
 10 should not be the center of a cell face. Indeed,  
 11 the spatial distribution of energy  $W_{\text{face } k}(\Omega_v, i, j)$   
 12 is not uniform on the exit face  $k$ . Moreover,  
 13 rays  $W_{\text{face } k}(\Omega_v, i, j)$  that exit face  $k$  have differ-  
 14 ent path lengths in the neighbor cells of the  
 15 emitting cell, which implies that the transmis-  
 16 sion of energy  $W_{\text{face } k}(\Omega_v, i, j)$ , starting from the  
 17 center of the face  $k$ , through several neighbor  
 18 turbid cells, differs from the sum of energies  
 19  $W_{\text{face } k}(\Omega_v, i, j)$  transmitted, after exiting face  $k$ .  
 20 Thus, for an upward direction in the Oyz  
 21 plan (Fig. 6), with cells close to the transmit-  
 22 ting cell characterized by a coefficient of pro-  
 23 jection  $G(\Omega_v)$  and a leaf volume density foliar  
 24  $u_{f''}$ , one has:

$$W_{\text{face } k}(\Omega_v) \cdot \exp[-G(\Omega_v) \cdot u_{f''} \cdot \Delta l_{\text{centre}}] \\ \neq < \sum_{i,j} W_{\text{face } k}(\Omega_v, i, j) \cdot \exp[-G(\Omega_v) \cdot u_{f''} \cdot \Delta l_{i,j}]$$

26  $\Delta l_{i,j}$  = distance from surface  $dS_{ij}$  to the hori-  
 27 zontal plane of the top face of the emitting  
 28 cell.

Tracking all individual rays requires much 29  
 computer resource. Thus, we developed a solu- 30  
 tion that is both accurate and efficient in terms 31  
 of computer time, for any type of turbid cell. It 32  
 determines a point  $P(X_P, Y_P, Z_P)$  such that the 33  
 energy  $W_{\text{face } k}(\Omega_v)$  transmitted from  $P$  through 34  
 several neighbor turbid cells is equal to the sum 35  
 of all individual energies  $W_{\text{face } k}(\Omega_v, i, j)$  trans- 36  
 mitted. For example, for the right vertical face 37  
 A (Fig. 6), co-ordinates  $X_P$  and  $Z_P$  of  $P$  verify 38  
 the two equations: 39

– coordinate  $X_P$ : 40

$$W_{\text{face } k} \times \exp(-G(\Omega_v) \times u_{f''} \times Lx_P) \\ = \iint_S (W(x, z, \Omega_v, u_f, \text{LAD}, T, \lambda) \\ \times \exp(-G(\Omega_v) \times u_{f''} \times Lx) \cdot dS)$$

– coordinate  $Z_P$ : 42

$$W_{\text{face } k} \times \exp(-G(\Omega_v) \times u_{f''} \times Lz_P) \\ = \iint_S (W(x, z, \Omega_v, u_f, \text{LAD}, T, \lambda) \\ \times \exp(-G(\Omega_v) \times u_{f''} \times Lz) \cdot dS)$$

$Lz_P$ : distance along  $(\Omega_v)$  between a point  $P$  of 44  
 face  $K$  and the horizontal plane that con- 45  
 tains the upper or lower face of the emit- 46  
 ting cell, depending if  $(\Omega_v)$  is upward or 47  
 downward. 48

$Lx_P$ : distance along  $(\Omega_v)$  between a point  $P$  of 49  
 face  $K$  and the vertical plane that contains 50

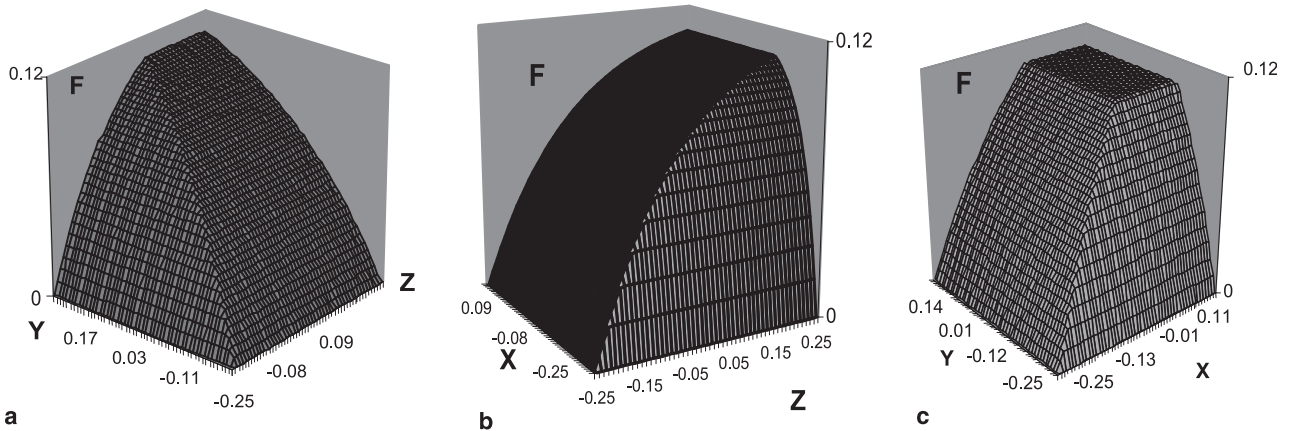


**Fig. 8.** 3-D relative distributions of the energy emitted by the faces of a turbid cell. (a) Front face ( $x = \Delta X$ ):  $F(y, z, \text{LAI}, \text{LAD})$ . (b) Right face ( $y = \Delta Y$ ):  $F(x, z, \text{LAI}, \text{LAD})$ . (c) Top face ( $z = \Delta Z$ ):  $F(x, y, \text{LAI}, \text{LAD})$ . LAI = 5.  $\Delta Y = \Delta Z = 0.5$ . LAD spherical.  $(\theta_v, \theta_v) = (60, 72)$

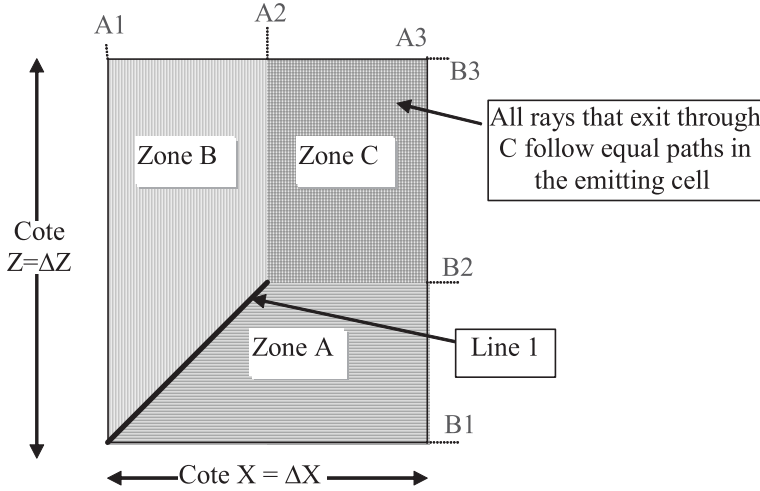


**Fig. 9.** 3-D schematic representation of distribution F

1 the front or back face of the cell, depending  
 2 if  $(\Omega_v)$  goes forward or backward.  
 3  $u_f$ : leaf volume density of the first cell crossed  
 4 by the ray from  $P$  along  $(\Omega_v)$ . It can be  
 5 null.

6 The energy emitted by a cell along  $(\Omega_v)$   
 7 through face  $k$  is proportional to " $L_B(\lambda, T) \times$   
 8 cross section  $dS_{\text{eff}}$  of face  $k$  along  $(\Omega_v)$ ". Position  
 9 of  $P$  on face  $k$  depends on the relative directional  
 10 distribution  $F$  of the energy emitted by the cell.  
 11 For the cell face in the plane  $\{y = \Delta Y\} > 0$ , this  
 12 distribution is:

$$F(x, z, \theta_v, \varphi_v, u_f, \text{LAD}) = \frac{W(x, z, \theta_v, \varphi_v, u_f, \text{LAD}, T, \lambda)}{L_B(\lambda, T) \times dS_{\text{eff}}}$$

14 Figure 8 shows the relative distribution  $F$   
 15 of the emitted energy through the front, right  
 16 and top faces of an emitting turbid cell  
 17 ( $\text{LAI} = 5$ ,  $\Delta Y = \Delta Z = 0.5$ , spherical LAD),  
 18 for direction  $(\theta_v, \varphi_v) = (60, 72)$ . Face center  
 19  $(x, y, z \in [-0.25, 0.25])$  is the origin of co-ordinates.  
 20  $F$  appears to be the juxtaposition of 3  
 21 zones (A, B, C) with generic shapes (Fig. 9)  
 22 the limits of which are exponential curves.  $F$   
 23 is constant in zone C and has an exponential  
 24 surface in zones A and B. These surfaces tend  
 25 to be plane surfaces if LAI becomes small.  
 26 They are characterized by 6 parameters (A1,  
 27 A2, A3, B1, B2, B3) that depend on  $(u_f,$   
 28 LAD,  $\Omega_v, k)$  values. These remarks suggest re-  
 29 placing the integral expressions of  $F$  by analyti-  
 30 cal expressions.

The case 'face  $y = \Delta Y$ ' is analyzed.  $F(x, z,$  31  
 LAI, LAD expressions differ in zones A, B and C: 32

–  $M(x, z)$  in zone A ( $z < B2$  and  $z < a \cdot (x +$  33  
 $\frac{\Delta X}{2}) - \frac{\Delta Z}{2}$ ): 34

$F_A(x, z, \text{LAI}, \text{LAD})$

$$= \frac{\omega \cdot [1 - \exp\left\{-\text{sign} e2 \cdot \text{LAI} \cdot \frac{(z - B1)}{|a|}\right\}]}{1 - \exp\left\{-\text{sign} e2 \cdot \text{LAI} \cdot \frac{(B3 - B1)}{|a|}\right\}}$$

–  $M(x, z)$  in zone B ( $x < A2$  and  $z < a \cdot (x +$  36  
 $\frac{\Delta X}{2}) - \frac{\Delta Z}{2}$ ): 37

$F_B(x, z, \text{LAI}, \text{LAD})$

$$= \frac{\omega \cdot [1 - \exp\{-\text{sign} e1 \cdot \text{LAI} \cdot (x - A1)\}]}{1 - \exp\{-\text{sign} e1 \cdot \text{LAI} \cdot (A3 - A1)\}}$$

–  $M(x, z)$  in zone C ( $x \in [A2, A3]$  and  $z \in$  39  
 $[B2, B3]$ ):  $F_C(x, z, \text{LAI}, \text{LAD}) = \omega$  40

$\text{sign} e1 = \text{sign}(A3 - A1)$

$\text{sign} e2 = \text{sign}(B3 - B1)$

$$a = \frac{B2 - B1}{A2 - A1} \quad u_f = \frac{\text{LAI}}{\Delta Z}$$

$$\omega = \Delta\Omega_v \cdot (1 - \exp(-G \cdot u_f \cdot L))$$

$d\Omega_v$ : solid angle of direction  $\Omega_v$ . 42

$L$ : longer path length of a ray within a cell. 43

$a$ : parameter that allows to ensure the continu- 44  
 ity of curves  $F_A$  and  $F_B$  45

Function  $F$  is not appropriate if the direction 46  
 of emission  $\Omega_v$  is parallel with a face (e.g., 47

1  $\varphi = 90^\circ$ ). Then, the emission along  $\Omega_v$  comes  
 2 only from 1 or 2 faces (e.g.,  $\theta = 0$ ,  $\varphi = 0$ ).

3 Calculation of the 3 co-ordinates of a point ori-  
 4 gin  $P$  on a cell face, requires to integrate  $F$  and to  
 5 verify some equations. For example, for the right  
 6 face of the cell ( $y = \Delta Y$ ), we must have:

$$W_{\text{face}} \times \exp(-G \cdot u_{f''} \cdot Lx_P) \\ = \iint_{\text{face}} (F_A + F_B + F_C) \cdot L_B(\lambda, T) \\ \cdot \exp(-G \cdot u_{f''} \cdot Lx) dS_{\text{eff}}$$

$$W_{\text{face}} \times \exp(-G \cdot u_{f''} \cdot Lx_P) \\ = \iint_{\text{face}} (F_A + F_B + F_C) \cdot L_B(\lambda, T) \\ \cdot \exp(-G \cdot u_{f''} \cdot Lz) dS_{\text{eff}}$$

9 Using:

$$Lx = \frac{(-\text{sign } e(\sin \theta \cdot \cos \varphi)) \cdot \text{Cote } X/2 - x}{\sin \theta \cdot \cos \varphi} \\ = \frac{\varepsilon_1 \cdot \text{Cote } X/2 - x}{\sin \theta \cdot \cos \varphi} \quad \text{with}$$

$$\varepsilon_1 = -\text{sign}(\sin \theta \cdot \cos \varphi)$$

$$Lz = \frac{(\text{sign } e(\cos \theta)) \cdot \text{Cote } X/2 - x}{\cos \theta} \\ = \frac{\varepsilon_3 \cdot \text{Cote } X/2 - x}{\cos \theta} \quad \text{with } \varepsilon_3 = \text{sign}(\cos \theta)$$

$$Ly = \frac{(-\text{sign } e(\sin \varphi \cdot \sin \theta)) \cdot \text{Cote } Y/2 - y}{\sin \varphi \cdot \cos \theta} \\ = \frac{\varepsilon_2 \cdot \text{Cote } Y/2 - y}{\sin \varphi \cdot \sin \theta} \quad \text{with}$$

$$\varepsilon_1 = -\text{sign}(\sin \theta \cdot \cos \varphi)$$

12 co-ordinates of  $P$  on the right face of the cell,

13 relative to the center of this cell, are:

$$x_P = \varepsilon_1 \cdot \text{Cote } X/2 + \frac{\cos \varphi \cdot \sin \theta}{G \cdot u_{f''}}$$

$$\cdot \ln \left( \frac{\iint_{\text{Zone A}} F_A \cdot L \cdot \exp(-G \cdot u_{f''} \cdot Lx) dS_{\text{eff}} + \iint_{\text{Zone B}} F_B \cdot L \cdot \exp(-G \cdot u_{f''} \cdot Lx) dS_{\text{eff}} + \iint_{\text{Zone C}} F_C \cdot L \cdot \exp(-G \cdot u_{f''} \cdot Lx) dS_{\text{eff}}}{W_{\text{face}}} \right)$$

$$z_P = \varepsilon_3 \cdot \text{Cote } Z/2 + \frac{\cos \theta}{G \cdot u_{f''}}$$

$$\cdot \ln \left( \frac{\iint_{\text{Zone A}} F_A \cdot L \cdot \exp(-G \cdot u_{f''} \cdot Lz) dS_{\text{eff}} + \iint_{\text{Zone B}} F_B \cdot L \cdot \exp(-G \cdot u_{f''} \cdot Lz) dS_{\text{eff}} + \iint_{\text{Zone C}} F_C \cdot L \cdot \exp(-G \cdot u_{f''} \cdot Lz) dS_{\text{eff}}}{W_{\text{face}}} \right)$$

Expressions of  $x_P$ ,  $y_P$  and  $z_P$  are very interesting 14  
 because they are analytical, which makes it pos- 15  
 sible to calculate them with small computation 16  
 times, for any configuration. 17

If there are  $\mathcal{T}$  leaf species, for each direction 18  
 ( $\Omega_v$ ) and each cell face, the point  $P$  is the center 19  
 of gravity of all  $\mathcal{T}$  points, weighted by the leaf 20  
 volume densities  $u_{f,t}$ . 21

## 5.2 Opaque surfaces 22

For an opaque surface of direct-hemispheric re- 23  
 flectance  $\rho_{\text{dh}}(\lambda, T, \Omega_v) : \alpha_a(\lambda, T, \Omega_v) = 1 - \rho_{\text{dh}}(\lambda, 24$   
 $T, \Omega_v)$ . Moreover,  $\rho_{\text{dh}}(\lambda, T, \Omega_v) = \rho_{\text{hd}}(\lambda, T, \Omega_v)$ . 25  
 Thus, with thermodynamic balance, in the ab- 26  
 sence of mechanisms of energy exchange other 27  
 than radiative (Hapke 1993), the emissivity is: 28

$$\varepsilon_d(\lambda, T, \Omega_v) = \alpha_a(\lambda, T, \Omega_v) = 1 - \rho_{\text{hd}}(\lambda, T, \Omega_v)$$

• Lambertian  $\rho_{\text{lamb}}$  + specular  $\rho_{\text{spe,dh}}(\Omega) : \varepsilon_d(\lambda, T, 30$   
 $\Omega_v) = 1 - \rho_{\text{lamb}} - \rho_{\text{spe,dh}}(\Omega_v)$  31

• Hapke  $\langle \rho \rangle$  + specular  $\rho_{\text{spe,dh}}(\Omega) : \varepsilon_d(\lambda, T, \Omega_v) = 32$   
 $1 - \langle \rho \rangle - \rho_{\text{spe,dh}}(\Omega_v)$  33

We consider only the outwards emission, and 34  
 not the inwards emission, by scene elements 35  
 made of opaque figures. Thus, the internal emis- 36  
 sion of houses is not introduced. This choice is 37  
 explained by the fact that DART is mostly dedi- 38  
 cated to the simulation of radiative transfer for 39  
 remote sensing purpose and for the radiative bud- 40  
 get of external surfaces of canopies. 41

Thus, a surface  $(S, \Omega_n, \varepsilon_d)$  emits only in the 42  
 hemisphere that contains its normal  $(\Omega_n)$ : 43

$$W_e(\lambda, T, \theta_v) \cong \varepsilon_d \cdot L_B(\lambda, T) \times S \times \cos \psi_{nv} \\ \times \Delta \Omega_v \quad \text{if } \psi_{nv} \leq 90$$

$$W_e(\lambda, T, \theta_v) \cong 0 \quad \text{if } \psi_{nv} \geq 90$$

$$\cos \psi_{nv} = \cos \theta_n \cdot \cos \theta_v + \sin \theta_n \\ \cdot \sin \theta_v \cdot \cos(\psi_{nv})$$

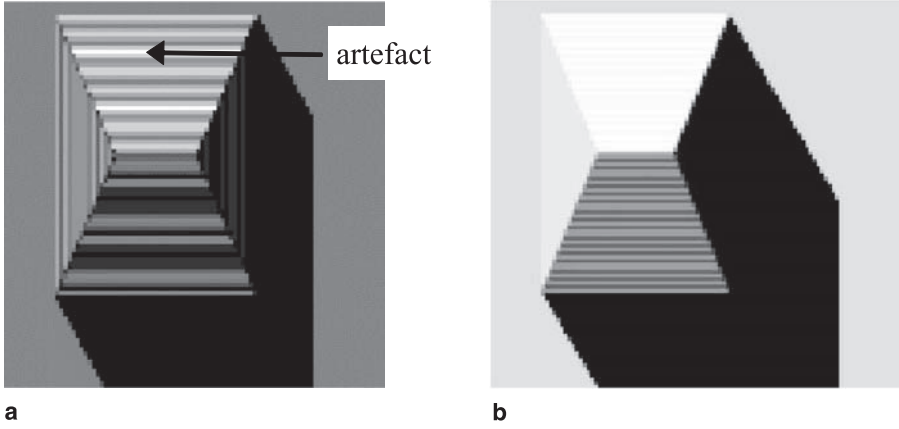


**Fig. 10.** Computation of  $T_{\text{figure}}$ , without (a) and with (b) account of the area of figures

1 Once emitted by a cell, a ray  $W(\Omega_v)$  is tracked in  
2 the 3D scene, where it can be:

- 3 • completely intercepted by an opaque surface,  
4 to be scattered in the following iteration, or.
- 5 • partly intercepted by turbid cells or not in-  
6 tercepted at all. Part of  $W(\Omega_v)$  that reaches a  
7 cell  $(\Delta X, \Delta Y)$  of scene top layer, increases the  
8 energy  $W_{\text{c-fict}}(\Omega_v)$  already stored by this cell.

9 After the last iteration,  $W_{\text{c-fict}}(\Omega_v)$  is translated  
10 into scene brightness temperature  $T_B(\Omega_v)$ .

$$T_B(\theta_v) = \frac{h \cdot C / \lambda \cdot k}{\ln \left( \frac{2 \cdot h \cdot C^2}{\lambda_o^5 \cdot (W_{\text{c,lop}}(\Omega_v) / \cos(\theta_v) \times \Delta\Omega_v \times \Delta X \times \Delta Y) + 1} \right)}$$

11 In the case of a simulation with  $\Delta\lambda \approx 0$ ,  $\lambda_o$  is  
12 the mean wavelength. This choice is not possible  
13 if  $\Delta\lambda \neq 0$ . In that case, the inversion is con-  
14 ducted with a reference wavelength that depends  
15 on the scene mean temperature  $T_{\text{mean}}$  (Dallhuin  
16 2002).  $\lambda_o$  verifies:

$$L_B(\lambda_o, T_{\text{mean}}) = \frac{1}{\Delta\lambda} \cdot \int_{\lambda_{\min}}^{\lambda_{\max}} L(\lambda, T_{\text{mean}}) \cdot d\lambda \\ \neq L \left( \frac{\lambda_{\min} + \lambda_{\max}}{2}, T_{\text{mean}} \right)$$

18 Two approaches can be used to specify the 3D  
19 temperature of the scene:

- 20 – 3D matrix of cell temperature values. This ma-  
21 trix can be computed by the DARTEB model  
22 (see last chapter). In that case, TIR emission  
23 of any opaque figure is simulated from the  
24 “geometric” barycentre of that figure.

- scene illumination in the visible spectral do-  
25 main. The temperature of any scene element is  
26 proportional to visible scene irradiance and is  
27 within a pre-defined interval that is specific for  
28 each type of scene element: soil, wall, roof,  
29 etc. The limited number of rays that simulate  
30 scene illumination necessarily introduces arti-  
31 facts. These are reduced (1) using a larger  
32 number of illuminating rays per cell of the  
33 scene upper layer (pre defined number is 49),  
34 (2) by accounting the area of each emitting  
35

opaque figure (Fig. 10) for calculating its tem-  
36 perature  $T_{\text{figure}}$ , and (3) by equalizing the tem-  
37 perature of all coplanar figures in the same  
38 cell. TIR emission of opaque figures is simu-  
39 lated from the “energy” barycentre for illu-  
40 minated figures, and from the “geometric”  
41 barycentre for “non illuminated figures”.  
42

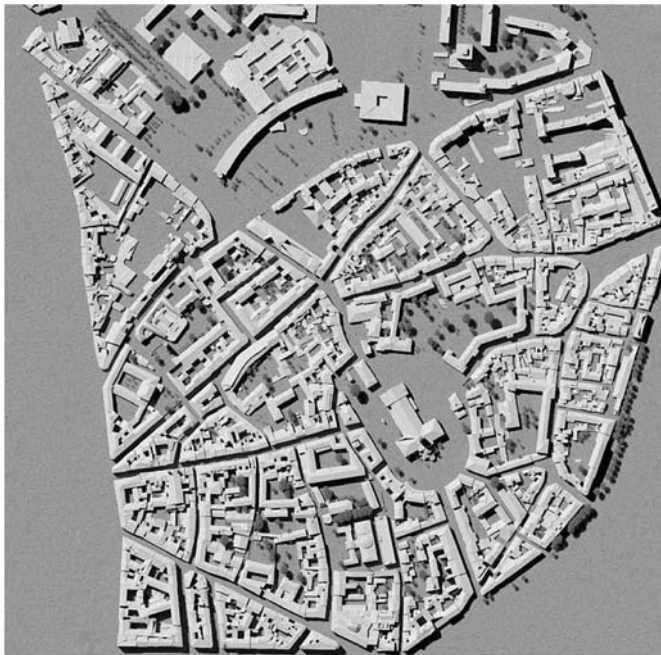
## 6. Application to CAPITOU project

43

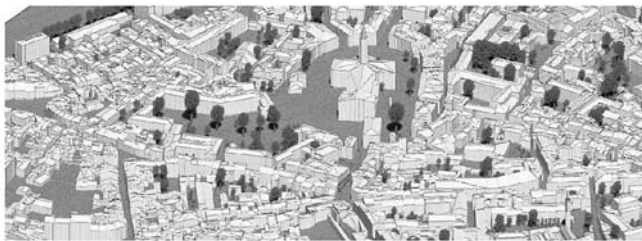
The new DART model was used in the context of  
44 the CAPITOU experiment that took place over  
45 the city of Toulouse, France, from February 2004  
46 to February 2005. Study of urban energy balance  
47 was one of the objectives. For that, different  
48 types of measurements took place: acquisition  
49 of TIR airborne images, in-situ measurements  
50 of turbulent fluxes, surface energy balance, sur-  
51 face temperatures, etc. (Masson et al. 2007).  
52

1 DART was used for simulating both remote  
 2 sensing images in visible, NIR and TIR spectral  
 3 bands and the 3D radiative budget. Moreover, the  
 4 DARTEB model used this simulated radiative  
 5 budget for assessing the time evolution of surface  
 6 variables such as wall temperatures and heat sen-  
 7 sible fluxes. DARTEB is a model that is being  
 8 developed for calculating the 3D (3 dimensional)  
 9 energy budget of urban and natural scenes,

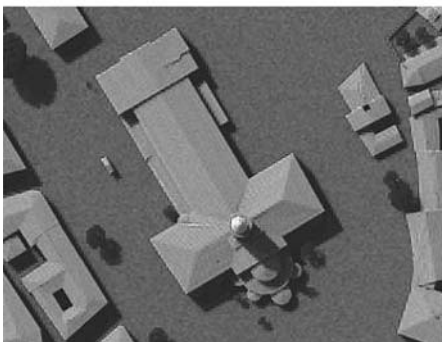
possibly with topography and atmosphere. It ac- 10  
 counts for all energy mechanisms (heat conduc- 11  
 tion, turbulent momentum and heat fluxes, water 12  
 reservoir evolution, vegetation photosynthesis, 13  
 evapotranspiration) that contribute to the energy 14  
 budget. In the case of a urban canopy, it simulates 15  
 non radiative mechanisms with the equations of 16  
 the TEB urban surface scheme (Masson 2000). 17  
 This scheme works with a canyon geometry. 18



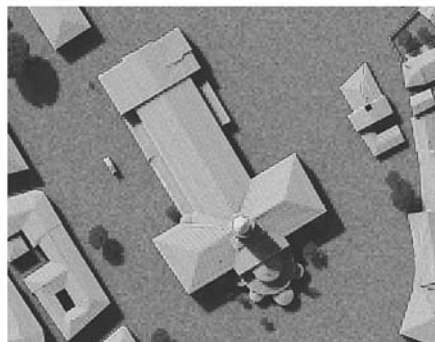
a



b



c



d

**Fig. 11.** DART simulated nadir (a) and oblique (b) images of St Sernin district. (c) and (d) show the St Sernin basilica (centre (a)) for a sensor below and on top of the atmosphere. Red spectral band

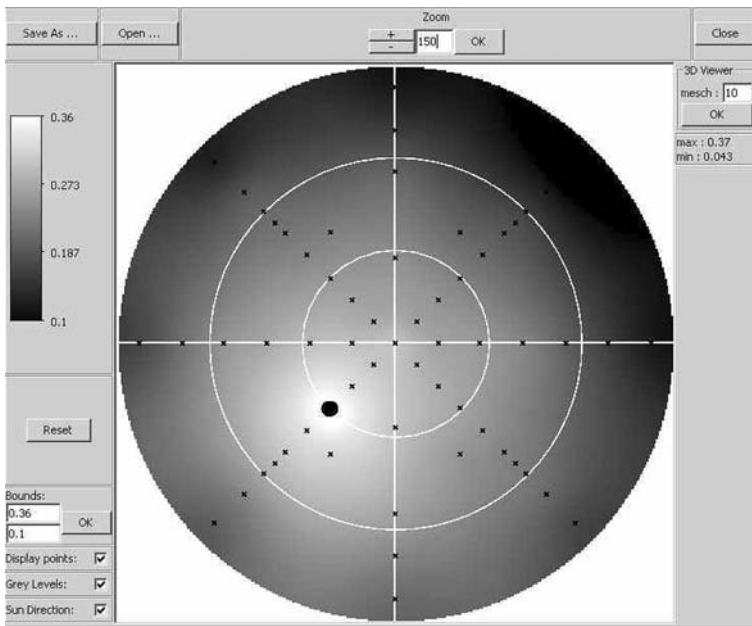


**Fig. 12.** Example of near infrared BRF of St Sernin district. It is computed by the DART graphic user interface with simulated reflectance values (crosses), for a sun direction shown by a black circle. Distance from the circle centre gives the view zenith angle ( $[0\ 90^\circ]$ ) and the anti clockwise angle from the horizontal axis gives the azimuth view angle ( $[0\ 360^\circ]$ )

### 1 6.1 DART simulated remote sensing images

2 First, a program was developed for importing the  
 3 urban database (Autocad format) of the Toulouse  
 4 town hall as a DART scene. This led to the crea-  
 5 tion of DART objects (e.g., houses and trees).  
 6 The fact that urban elements in the data base  
 7 are not houses or buildings but unrelated individ-  
 8 ual walls and roofs was a difficulty. The local  
 9 digital elevation model (DEM) was also import-  
 10 ed. Figure 11 shows nadir (a) and oblique (b)  
 11 color composites of the St Sernin district of  
 12 Toulouse city. They were created with DART  
 13 simulations in the blue, green and red spectral  
 14 bands. Simulations stress that urban reflectance  
 15 and brightness temperature values display a  
 16 marked angular heterogeneity. This heterogene-  
 17 ity is illustrated here with the angular distribu-  
 18 tion of NIR reflectance values of St Sernin district  
 19 (Fig. 12).

20 Figure 11c and d display DART remote sens-  
 21 ing images of St Sernin basilica, in the center of  
 22 St Sernin district. They are simulated for a sensor  
 23 at the bottom of the atmosphere (i.e., BOA im-  
 24 age) and for a sensor at the top the atmosphere  
 25 (TOA). The bluish tone of the TOA image, com-  
 26 pared to the BOA image, is due to the fact that  
 27 atmosphere scatters more in the blue than in  
 28 the red spectral domain. The realistic aspect of  
 29 DART images is encouraging. However, the ob-  
 30 jective of DART is to simulate satellite images

with accurate geometric and radiometric charac- 31  
 32 teristics. This is necessary for studying Earth sur- 33  
 34 faces from space, using a physical approach such 35  
 36 as image inversion (Gastellu-Etchegorry et al. 37  
 38 2003). Although DART was already validated for 38  
 39 the visible and NIR spectral domains (Widlowski 39  
 40 et al. 2007) and partly validated for the TIR do- 40  
 41 main (Guillevic et al. 2003), in the future, it should 41  
 42 be also validated for TIR radiative transfer in ur- 42  
 43 ban canopies with satellite images. 43

### 44 6.2 DARTEB energy budget simulation 41

42 DARTEB simulates the energy budget of urban 42  
 43 and vegetation canopies. For that, it uses the 3-D 43  
 44 DART radiative budget and it models all physical 44  
 45 phenomena, other than radiation, that contribute 45  
 46 to the energy budget. In the case of urban cano- 46  
 47 pies, turbulent fluxes and conduction are compu- 47  
 48 ted with classical boundary-layer laws using 48  
 49 equations of the TEB model (Masson 2000). 49  
 50 However, conversely to TEB model DARTEB 50  
 51 uses a 3-D cell discretization, in addition to the 51  
 52 layer discretization of roofs, walls and roads: 52  
 53 modeling is conducted on a DART cell per cell 53  
 54 basis. As a result, fluxes are computed for each 54  
 55 point of the 3-D scene. The transfer coefficients 55  
 56 for turbulent heat and moisture fluxes are identi- 56  
 57 cal; they differ from the transfer coefficients for 57  
 58 momentum fluxes. For DARTEB, the urban can- 58



1 opy is simulated as the juxtaposition of urban  
 2 street canyons. Here, we worked with a single  
 3 urban canyon (Fig. 13), for remaining in the va-

4 lidity domain of TEB equations (Masson 2000).  
 5 Most major variables used by DARTEB are men-  
 6 tioned in Fig. 13. Each surface type (wall, soil,

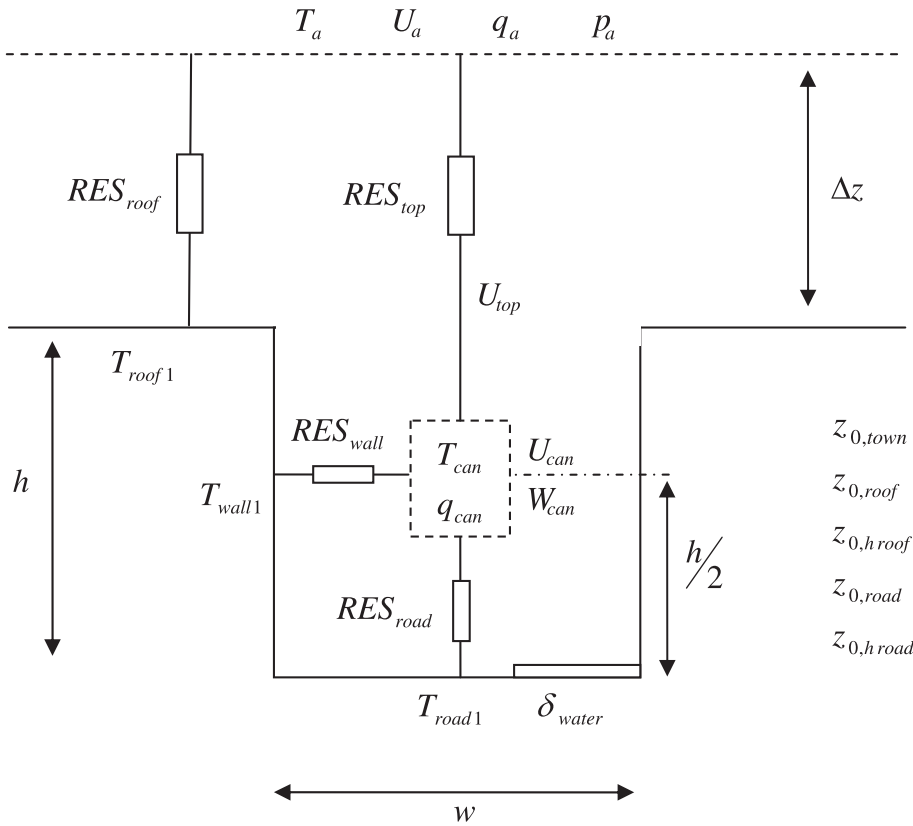


**Fig. 13.** Simulation of the canyon. Parameters used by DARTEB are listed below.  $U_a, T_a, q_a, p_a$ : Wind speed and air temperature/humidity/pressure at 1st atmosphere layer.  $h, w$ : Canyon height and width.  $\Delta_z$ : Height of measurements above the roof,  $U_{top}$ : wind speed right above the canyon.  $T_{roof1}, T_{wall1}, T_{road1}$ : Roof, wall and road temperatures.  $RES_{top}/RES_{roof}$ : Aerodynamic resistance between the atmosphere and the canyon/roof,  $RES_{wall}/RES_{road}$ : Aerodynamic resistance between the canyon and the wall/road,  $U_{can}/W_{can}, T_{can}, q_{can}$ : Canyon horizontal/vertical wind speed and air temperature/humidity,  $z_{0,roof}, z_{0,h roof}, z_{0,road}, z_{0,h road}$ : Roof and road dynamic and thermal roughness lengths.  $z_{0,town}$ : Town dynamic roughness length.  $\delta_{eau}$ : Percentage of wet road

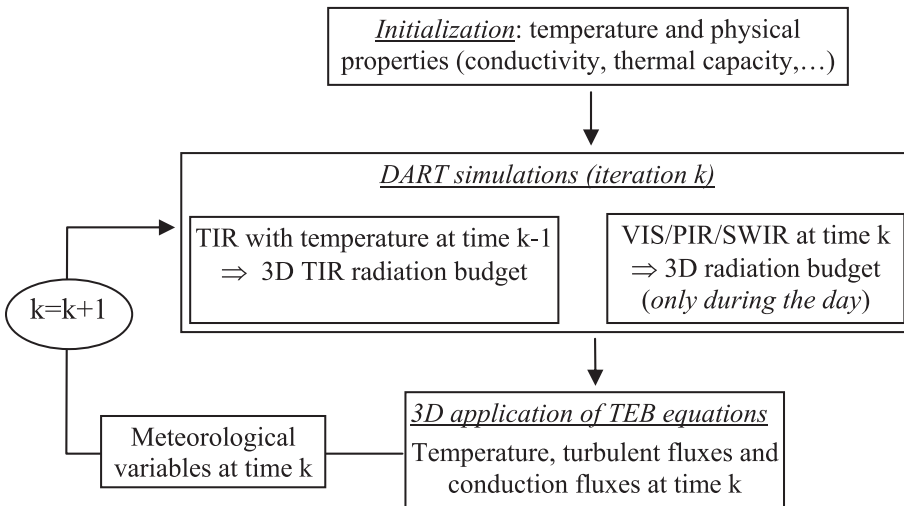


**Fig. 14.** Diagram of DARTEB model

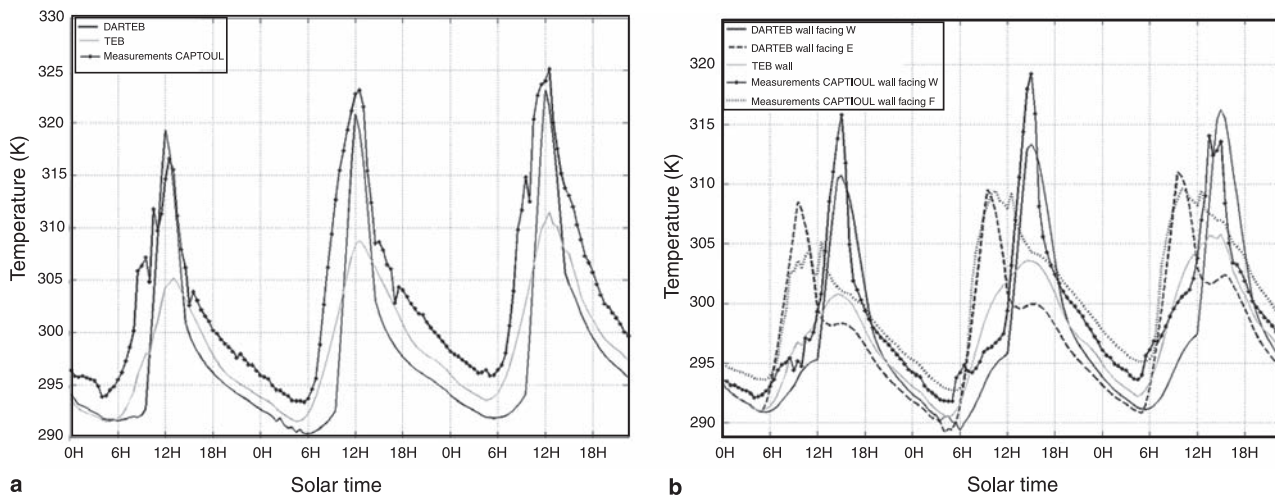


**Fig. 15.** Comparison of temperature measurements with DARTEB and TEB simulations. July 14–16 2004. (a) Road of La Pomme street (Toulouse) with a south East – North West orientation. (b) Walls of Alsace Lorraine street (Toulouse) with a South-North orientation. The 2 walls are facing West and East directions, which implies different thermal behaviors

1 roof) is discretized into several layers for simulating the conduction fluxes to or from the ground and building interiors. The number of layers for road, wall and roof can differ. A minimal number of three layers is advised because temperature gradients can be large and because of the multi-layer structure of the walls and roofs.

9 DARTEB uses a prognostic approach (Fig. 14) for assessing the 3D radiative budget distribution, and consequently the 3D temperature distribution. Temperature values at time “ $k-1$ ” are used for computing the 3D TIR and energy budgets at time “ $k$ ”, which allows one to compute the 3D temperature distribution at time “ $k$ ”, using the 3D visible and NIR radiation budget at time “ $k$ ” (Fig. 14). DART simulations in the short wave domain are conducted during the day period only.

20 The validity of DARTEB was tested against TEB simulations and against in situ temperature measurements during the Capitoul campaign (Albinet 2008). DARTEB proved to be coherent with TEB and with measurements. Here, this is illustrated by the comparison of simulated and measured temperatures during 3 days, from July 27 14 to July 17, 2004, for the Alsace Lorraine street (South-North orientation) and La Pomme street (South East – North West orientation) in Toulouse.

The simulated and measured road temperature curves are very similar (Fig. 15a). As expected, road temperature values increase during the day. There are 3 major differences between DARTEB and TEB simulations. (1) Maximal DARTEB temperatures are larger than maximal TEB temperatures. (2) Maximal DARTEB temperatures occur before midday conversely to maximal TEB temperatures that occur at midday. (3) DARTEB curves are smoother than TEB curves. These differences are mostly explained by the fact that DARTEB takes into account the 3-D nature of the canyon geometry, conversely to TEB.

Indeed, the TEB model works with a mean canyon that corresponds to an azimuthally averaged street direction. Thus, TEB temperatures are mean values, which explains that their time variations are smoothed, with maximal values at midday. Actually, due to the South East – North West orientation of La Pomme street, the maximum road illumination occurs before midday and the maximal road illumination is larger than the mean road illumination for all possible canyon orientations. This is well simulated by DARTEB. Each morning, the measured and DARTEB temperature values display nearly the same sharp increase. However, each afternoon, DARTEB temperature values decrease faster than TEB and the observed temperature values. Several factors can explain the differences be-

1 tween the DARTEB and observed temperature  
 2 values. For example, an inaccurate road heat ca-  
 3 pacity implies an inaccurate conduction flux, and  
 4 an inaccurate road roughness length tends to im-  
 5 ply an inaccurate heat flux, which tends to lead to  
 6 inaccurate road temperature values. Another possi-  
 7 ble explanation can come from an inaccurate  
 8 simulation of the proportions of the 2 compo-  
 9 nents of the canyon illumination: sun and sky  
 10 illumination. Here, these components are driven  
 11 by the atmosphere optical depth and sun zenith  
 12 angle. However, in the absence of measurements,  
 13 the atmosphere optical depth is assumed to be  
 14 constant.

15 The wall (Fig. 15b) DARTEB and measured  
 16 temperature values tend to be very close, both  
 17 for the wall facing West, and for the wall facing  
 18 East. They differ from TEB temperature values  
 19 because TEB gives a mean value for the 2 walls  
 20 of the canyon. Account of wall orientation is im-  
 21 portant because walls with different sun illumi-  
 22 nation have different temperature values, with  
 23 larger values during daytime for walls with best  
 24 sun orientation. As expected, DARTEB maximal  
 25 temperature values occur in the morning for the  
 26 wall facing East, and in the afternoon for the wall  
 27 facing West. This is not the case with TEB maxi-  
 28 mal temperature values; they occur at midday  
 29 due to the fact that TEB works with azimuthally  
 30 averaged canyons. This explains also that TEB  
 31 temperature values are too small. These exam-  
 32 ples stress the impact of 3-D architecture on tem-  
 33 perature distributions.

## 34 7. Conclusion

35 Some major and recent improvements of DART  
 36 radiative transfer model are presented in this pa-  
 37 per. Thanks to these improvements, the DART  
 38 model can simulate the radiation budget and re-  
 39 mote sensing images of urban and natural land-  
 40 scapes, with atmosphere and topography. Urban  
 41 landscapes are simulated as the juxtaposition  
 42 of opaque figures (i.e., triangles and parallelo-  
 43 grams). A few basic urban elements are pre-de-  
 44 fined for easing the building of urban landscapes:  
 45 houses with different roofs, low walls, roads,  
 46 etc. Opaque figures are characterized by spe-  
 47 cific optical properties: lambertian, specular or  
 48 Hapke reflectance/emissivity. In order to im-  
 49 prove DART radiometric accuracy, the origin of

the path of any scattered and/or emitted ray is 50  
 either a sub-cell center or a cell sub-face center. 51

In order to avoid repetitive calculations when 52  
 simulating radiative transfer, which is costly in 53  
 terms of computation time, some components of 54  
 the emission by turbid cells and opaque figures 55  
 are pre-computed. For example, the intensity that 56  
 turbid cells emit is pre-computed for each turbid 57  
 cell type (i.e.,  $\rho_f$ ,  $\tau_f$ , LAD), for each cell face, for 58  
 a range of volume density values  $u_f$ , and for 59  
 each direction  $\Omega_v$ . Moreover, emitted rays start 60  
 from a point on cell faces, with a location that 61  
 is analytically computed using pre-computed 62  
 parameters that depend on the characteristics of 63  
 the emitting cell and of cells that bound the emit- 64  
 ting cell. 65

DART was used in the context of the Capitoul 66  
 project (Masson et al. 2007). The objective was 67  
 to test its potential for simulating remote sensing 68  
 images and the radiation budget of urban cano- 69  
 pies. For that, the Toulouse urban database was 70  
 imported as a DART scene. Resulting simulated 71  
 satellite images stressed the potential of DART 72  
 for urban studies using remote sensing measure- 73  
 ments. Moreover, DART simulated 3D radiation 74  
 budget proved to be a valuable input for model- 75  
 ing the 3D energy budget and heat fluxes with the 76  
 DARTEB model. Results show that DARTEB 77  
 simulated temperature values compare very well 78  
 with in situ measurements, with results even bet- 79  
 ter than TEB model. These better results are 80  
 surely due to the fact that the DARTEB radiation 81  
 budget is more accurate than the TEB radiation 82  
 budget. Moreover, the DARTEB 3-D calculation 83  
 of fluxes (i.e., on a cell per cell basis) affects 84  
 also results. Work is being continued for better 85  
 understanding differences between DARTEB 86  
 and in situ measurements and TEB simulations 87  
 on the other hand. An important objective is 88  
 to determine in which case the account of 3D 89  
 information, instead of 2D information as in 90  
 the TEB scheme, is needed for accurate urban 91  
 studies. 92

The DART code with the above mentioned 93  
 improvements was recently professionalized by 94  
 Magellium ([www.magellium.fr](http://www.magellium.fr)) for Linux and 95  
 Window systems, with the support of French 96  
 Space Center (CNES). Work is still conducted 97  
 for obtaining a reference model for remote sens- 98  
 ing studies. DART is patented (PCT/FR 02/ 99  
 01181). Paul Sabatier University (France) pro- 100

1 vides free licenses for scientific works ([www.cesbio.ups-tlse.fr](http://www.cesbio.ups-tlse.fr)).

### 3 Annex

4 In DART model, there are 4 possible types of reflectance for  
5 the opaque surfaces.

6 • *Type 0*: “Lambertian + random spatial variability”.

$$\rho(\Omega_s, \Omega_v) = \rho_{\text{lamb}} + \text{standard deviation } \sigma\rho.$$

8 • *Type 1*: “Lambertian + specular reflectance  $\rho_{\text{spec}}(\Omega_s, \Omega_v)$ ”.

$$\rho(\Omega_s, \Omega_v) = \rho_{\text{lamb}} + \rho_{\text{spec}}(\Omega_s, \Omega_v)$$

10 DART discretization of directions complicates specular  
11 reflectance modeling because there may be no discrete direc-

This allows one to define the direct-hemispheric reflectance factor:

$$\rho_{\text{spe,dh}}(\Omega_s) = \frac{W_{\text{spe}}(\Omega_s)}{W_{\text{int}}(\Omega_s)} = \pi \cdot \left\{ \left[ \frac{\text{tg}(\theta_i - \theta_t)}{\text{tg}(\theta_i + \theta_t)} \right]^2 + \left[ \frac{\sin(\theta_i - \theta_t)}{\sin(\theta_i + \theta_t)} \right]^2 \right\} \cdot A \cdot \frac{\alpha^4}{64} \cdot \left[ 1 - \frac{\alpha^2}{72} \right]$$

A surface S illuminated by an isotropic radiance  $L$  intercepts  $W_{\text{int}}(\Omega_s) = \int L \cdot S \cdot \cos \theta_s \cdot d\Omega_s$ . DART discrete directions have small solid angles  $\Delta\Omega_i$ . Thus:

$$\sum_i \cos \theta_i \cdot \Delta\Omega_i = 2\pi \cdot \sum_i \cos \theta_i \cdot \sin \theta_i \cdot \Delta\theta_i \approx \pi.$$

This allows one to define the hemispheric-hemispheric reflectance factor:

$$\rho_{\text{spe,hh}}(\Omega_s) = \frac{\int W_{\text{spe}}(\Omega_s) \cdot d\Omega_s}{\int W_{\text{int}}(\Omega_s) \cdot d\Omega_s} \approx \frac{\sum_i \pi \cdot \left\{ \left[ \frac{\text{tg}(\theta_i - \theta_t)}{\text{tg}(\theta_i + \theta_t)} \right]^2 + \left[ \frac{\sin(\theta_i - \theta_t)}{\sin(\theta_i + \theta_t)} \right]^2 \right\} \cdot A \cdot \frac{\alpha^4}{64} \cdot \left[ 1 - \frac{\alpha^2}{72} \right] L \cdot S \cdot \cos \theta_i \cdot \Delta\Omega_i}{\sum_i L \cdot S \cdot \cos \theta_i \cdot \Delta\Omega_i}$$

$$\Rightarrow \rho_{\text{spe,hh}}(\Omega_s) \approx \pi \cdot A \cdot \frac{\alpha^4}{32} \cdot \left[ 1 - \frac{\alpha^2}{72} \right] \cdot \sum_i \left\{ \left[ \frac{\text{tg}(\theta_i - \theta_t)}{\text{tg}(\theta_i + \theta_t)} \right]^2 + \left[ \frac{\sin(\theta_i - \theta_t)}{\sin(\theta_i + \theta_t)} \right]^2 \right\} \cdot \cos \theta_i \cdot \sin \theta_i \cdot \Delta\theta_i$$

12 tion that coincides with the Fresnel specular direction; *i.e.* a  
13 direction that depends on the incident ray direction and on  
14 the scatterer orientation.

15 Specular energy scattered is assumed to occur in a cone  
16 of angular width  $\alpha$ , with a value  $W_{\text{spe}}(\Omega_v^*)$  along  $(\Omega_v^*)$  that  
17 decreases quadratically like “ $\left[ \frac{\alpha^2}{4} - \Psi_{\text{vv}^*}^2 \right]$ ” from the Fresnel  
18 specular direction. Its total value  $W_{\text{spe}}(\Omega_s)$  is assumed to be  
19 proportional to the intercepted incident radiation  $W_{\text{int}}(\Omega_s)$ , to  
20 the theoretical Fresnel reflectance (*i.e.*, function of the refrac-  
21 tion index  $n(\lambda)$ ) and to a weight A.

$$W_{\text{spe}}(\Omega_s) = \int_0^{\alpha/2} \frac{1}{2} \cdot \left\{ \left[ \frac{\text{tg}(\theta_i - \theta_t)}{\text{tg}(\theta_i + \theta_t)} \right]^2 + \left[ \frac{\sin(\theta_i - \theta_t)}{\sin(\theta_i + \theta_t)} \right]^2 \right\} \cdot A \cdot \left[ \frac{\alpha^2}{4} - \Psi_{\text{vv}^*}^2 \right] \cdot \sin \Psi_{\text{vv}^*} \cdot d\Psi_{\text{vv}^*} \cdot 2\pi \cdot W_{\text{int}}(\Omega_s)$$

23 where  $\theta_i$  and  $\theta_t$  are the zenith angles of the incident and  
24 refracted rays, with  $\sin \theta_t = n \cdot \sin \theta_i$

25 With  $\alpha \ll 1$ , we have  $\sin \Psi_{\text{vv}^*} = \Psi_{\text{vv}^*} - \frac{1}{6} \cdot \Psi_{\text{vv}^*}^3$  for all  
26 directions of the specular scattering cone. As a result:

$$W_{\text{spe}}(\Omega_s) = \pi \cdot W_{\text{int}}(\Omega_s) \cdot \left\{ \left[ \frac{\text{tg}(\theta_i - \theta_t)}{\text{tg}(\theta_i + \theta_t)} \right]^2 + \left[ \frac{\sin(\theta_i - \theta_t)}{\sin(\theta_i + \theta_t)} \right]^2 \right\} \cdot A \cdot \int_0^{\alpha/2} \left[ \frac{\alpha^2}{4} - \Psi_{\text{vv}^*}^2 \right] \cdot \left[ \Psi_{\text{vv}^*} \cdot \frac{1}{6} \Psi_{\text{vv}^*} \right] \cdot d\Psi_{\text{vv}^*}$$

$$W_{\text{spe}}(\Omega_s) = \pi \cdot W_{\text{int}}(\Omega_s) \cdot \left\{ \left[ \frac{\text{tg}(\theta_i - \theta_t)}{\text{tg}(\theta_i + \theta_t)} \right]^2 + \left[ \frac{\sin(\theta_i - \theta_t)}{\sin(\theta_i + \theta_t)} \right]^2 \right\} \cdot A \cdot \frac{\alpha^4}{64} \cdot \left[ 1 - \frac{\alpha^2}{72} \right]$$

Modeling multiple scattering by specular surfaces uses  $W_{\text{spe,hh}}(\Omega_s)$ . Indeed, for multiple scattering, specular surfaces are assumed to be lambertian with a reflectance coefficient equal to {lambertian reflectance  $\rho_{\text{lamb}}$  + average specular reflectance  $\rho_{\text{spe,hh}}$ }.

It results that  $W_{\text{spe}}(\Omega_s)$  is equal to the theoretical specular radiation (Fresnel) weighted by the factor  $\pi \cdot A \cdot \frac{\alpha^4}{32} \cdot \left[ 1 - \frac{\alpha^2}{72} \right]$ , usually less than 1. Being reflected in a cone of half angle  $\alpha/2$ , it must be distributed in all the  $\mathcal{D}$  angular sectors  $(\Omega_v, \Delta\Omega_v)$  that intersect the specular cone  $\Delta\Omega_v = 2\pi \cdot (1 - \cos \frac{\alpha}{2})$ . Source vectors  $W_{\text{spe}}(\Omega_v, \Delta\Omega_v)$  are computed for any direction  $(\Omega_v, \Delta\Omega_v)$  using the approximations and the algorithm presented below.

– Approximations used for ensuring:  $\sum_{\mathcal{D}} W_{\text{spe}}(\Omega_v, \Delta\Omega_v) = W_{\text{spe}}(\Omega_s)$ . 50 51

$$W_{\text{spe}}(\Omega_v, \Delta\Omega_v) \approx W_{\text{spe}}(\Omega_s) \cdot \frac{\Delta\Omega_v \cdot \left[ \frac{\alpha^2}{4} - \Psi_{\text{vv}^*}^2 \right]}{\sum \Delta\Omega_v \cdot \left[ \frac{\alpha^2}{4} - \Psi_{\text{vv}^*}^2 \right]}$$

if  $|\Psi_{\text{vv}^*}| < \frac{\alpha}{2}$  and  $\Delta\Omega'_v = \Delta\Omega_v \cap \text{specular cone}$

$$W_{\text{spe}}(\Omega_v, \Delta\Omega_v) = 0 \quad \text{if } |\Psi_{\text{vv}^*}| > \frac{\alpha}{2}$$

– Approximations used for avoiding to compute the intersection of solid angles 54 55

$$\Delta\Omega'_v = \Delta\Omega_v \quad \text{if } \left\{ \Delta\Omega_v < \Delta\Omega_v^* \quad \text{and} \quad |\Psi_{\text{vv}^*}| < \frac{\alpha}{2} \right\}$$

$$\Delta\Omega'_v = \Delta\Omega_v^* \quad \text{if } \left\{ \Delta\Omega_v > \Delta\Omega_v^* \quad \text{and} \quad |\Psi_{\text{vv}^*}| < \frac{\alpha}{2} \right\}$$

and  $\Delta\Omega'_v = 0$  if  $|\Psi_{\text{vv}^*}| > \frac{\alpha}{2}$

- 1 – Algorithm:
- 2 a) Determination of the angles  $(\theta_v^*, \phi_v^*)$  of the specular
- 3 direction  $(\Omega_v^*)$ :
- 4 Let  $\beta$  the angle between the surface normal  $\Omega_n$  and the
- incident direction  $\Omega_i$ . For any  $\Omega_i$ ,  $\beta = \theta_v^*$ , the vectors
- $\Omega_i$ ,  $\Omega_v^*$  et  $\Omega_n$  must be coplanar and the phase angle
- must verify  $(\Omega_i, \Omega_v^*) = 2 \cdot \beta$ . With the notation “ $\theta_s =$
- $\pi - \theta_i$ ,  $\phi_s = \phi_i$ ”,  $\Omega_v^*$  is calculated from:  $\Omega_v^* + \Omega_s =$
- $2 \cos \beta \Omega_n$
- 10 b) Determination of the  $\mathcal{D}$  directions that verify
- 11  $|\Psi_{vv^*}| < \frac{\alpha}{2}$ .
- 12 c) Calculation of  $\Delta \Omega_v' \cdot [\frac{\alpha^2}{4} - \Psi_{vv^*}^2]$  for every direction.
- 13 • *Type 2: “Hapke + specular”.*

$$\rho(\Omega_s, \Omega_v) = \rho_{\text{Hapke}}(\Omega_s, \Omega_v) + \rho_{\text{spec}}(\Omega_s, \Omega_v)$$

- 15 The component  $\rho_{\text{Hapke}}$  is calculated with a modeling
- 16 that assimilates an opaque figure to a plane medium made
- 17 of particles randomly distributed and large compared to
- 18 wavelength (Hapke 1993). The phase function  $P(g_1, g_2)$
- 19 of particles, fitted by a Legendre polynomial, simulates
- 20 backscattering and forward scattering (Jacquemoud et al.
- 21 1992). Phase angle  $g_1$  is defined as the angle between the
- 22 incident sun direction  $(\Omega_s)$  and the view direction  $(\Omega_v)$ .  $g_2$
- 23 is defined as the angle between the specular direction  $(\Omega_{v^*})$
- 24 and  $(\Omega_v)$ :

$$\rho_{\text{Hapke}}(\Omega_s, \Omega_v, \Omega_n) = \frac{\omega}{4} \cdot \frac{1}{\cos(\Psi_{in}) + |\cos(\Psi_{sn})|}$$

$$\cdot [[1 + B(g_1)] \cdot P(g_1, g_2)$$

$$+ H(\omega, |\cos(\Psi_{sn})|)$$

$$\cdot H(\omega, \cos(\Psi_{in}) - 1)]$$

$$B(g_1) = \frac{B_0}{1 + \frac{1}{h} \cdot \tan\left(\frac{g_1}{2}\right)} \quad H(\omega, x) = \frac{1 + 2 \cdot x}{1 + 2 \cdot \gamma \cdot x}$$

$$\gamma = (1 - \omega)^{0.5}$$

$$P(g_1, g_2) = 1 + b_1 \cdot \cos g_1 + c_1 \cdot \frac{3 \cdot \cos^2(g_1) - 1}{2}$$

$$+ b_2 \cdot \cos(g_2) + c_2 \cdot \frac{3 \cdot \cos^2(g_2) - 1}{2}$$

- 28  $B(g)$  simulates the hot spot with a height  $B_0$  and a width  $h$ .
- 29 Model “Hapke + specular” uses 12 parameters:
- $$\{\omega, B_0, h, b_1, c_1, g_1, b_2, c_2, g_2\} + \{A, \alpha, n\}$$

- 31 Multiple scattering is simulated using the assumption
- 32 that the surface is lambertian with a reflectance coeffi-
- 33 cient calculated by the *phase* module. For the Hapke
- 34 model with  $b_2 = c_2 = g_2 = 0$ , multiple scattering is cal-
- 35 culated with:

$$\langle \rho(\Psi_{nv}) \rangle = \frac{1 - (1 - \omega)^{0.5}}{1 + 2 \cdot (1 - \omega)^{0.5} \cdot \cos \Psi_{nv} + \rho_{\text{spe, hd}}(\Omega_v)}$$

- 37 • *Type 3: Functions  $T_d(\Omega_s, \Omega_v)$ ,  $T_{\text{spe}}(\Omega_s, \Omega_v)$  and  $T_{\text{pol}}(\Omega_s,$*
- 38  $\Omega_v)$  represent the total, specular and polarized reflectance.
- 39 They can be used with horizontal surfaces only.

## References

- Albinet C (2008) Modélisation 3D des flux et du bilan 41  
d’énergie des zones urbaines Modélisation des échanges 42  
d’énergie des milieux urbains. M2 report. Paul Sabatier 43  
University, Toulouse, France, 57pp 44
- Berk A, Bernstein LS, Robertson DC (1989) MODTRAN: 45  
a moderate resolution model for LOWTRAN 7, 46  
GL-TR-89-0122, Geophys. Lab., Bedford, MA, USA, 47  
38pp 48
- Boyat P (2001) Modélisation du transfert radiatif dans le 49  
domaine thermique des surfaces terrestres. Report. École 50  
Nationale Supérieure d’Ingénieurs de Constructions 51  
Aéronautiques, Toulouse, France, 85pp 52
- Dallest T (2001) Modélisation du transfert radiatif 53  
atmosphérique dans le domaine de l’infrarouge thermi- 54  
que. École Nationale Supérieure d’Hydraulique et de 55  
Mécanique de Grenoble. Report, France, 78pp 56
- Gascon F (2001) Modélisation Physique d’Images de 57  
Télétection Optique. PhD Thesis. Université Paul Saba- 58  
tier, Toulouse, France 59
- Gastellu-Etchegorry JP, Demarez V, Pinel V, Zagolski F 60  
(1996) Modeling radiative transfer in heterogeneous 61  
3-D vegetation canopies. Remote Sens Environ 58: 62  
131–56 63
- Gastellu-Etchegorry JP, Guillevic P, Zagolski F, Demarez 64  
V, Trichon V, Deering D, Leroy M (1999) Modeling 65  
BRF and radiation regime of tropical and boreal 66  
forests – BRF. Remote Sens Environ 68: 281–316 67
- Gastellu-Etchegorry JP, Gascon F, Estève P (2003) An 68  
interpolation procedure for generalizing a look-up table 69  
inversion method. Remote Sens Environ 87: 55–71 70
- Gastellu-Etchegorry JP, Martin E, Gascon F (2004) 71  
DART: a 3-D model for simulating satellite images 72  
and surface radiation budget. Int J Remote Sens 25(1): 73  
75–96 74
- Gentine P (2002) Amélioration des images simulées par 75  
DART. Report. École Nationale Supérieure de l’ 76  
Aéronautique et l’Espace, Toulouse, France, 75pp 77
- Govaerts Y, Verstraete MM (1998) Raytran. A Monte Carlo 78  
ray tracing model to compute light scattering in three- 79  
dimensional heterogeneous media. IEEE Trans Geosci 80  
Remote Sens 36: 493–505 81
- Grau E (2008) DART atmosphere radiative transfer model- 82  
ing, 2008 M2 report, CESBIO 83
- Guillevic P, Gastellu-Etchegorry JP (1999) Modeling 84  
BRF and radiation regime of tropical and boreal fore- 85  
sts – PAR regime. Remote Sens Environ 68: 317–40 86
- Guillevic P, Gastellu-Etchegorry JP, Demarty J, Prévot L 87  
(2003) Thermal infrared radiative transfer within three- 88  
dimensional vegetation cover, J Geophys Res Atmos 89  
ATMOSPH 108(D8); DOI: 10.1029/2002JD002247 90
- Hapke B (1993) Theory of reflectance and emittance spec- 91  
troscopy. Cambridge University Press, New York 92
- Jacquemoud S, Baret F, Hanocq JF (1992) Modeling spectral 93  
and bidirectional soil reflectance. Remote Sens Environ 94  
41: 123–32 95
- Kimes DS, Sellers PJ (1985) Inferring hemispherical reflec- 96  
tance of the Earth’s surface for global energy budgets 97

- 1 from remotely sensed nadir or directional radiance values.  
 2 Remote Sens Environ 18: 205–23
- 3 Malenovský Z, Martin E, Homolova L, Pokorný R,  
 4 Schaepman ME, Gastellu-Etchegorry J-P, Zurita Milla  
 5 R, Clevers JGPW, Cudlin P (2005) Influence of forest  
 6 canopy structure simulated using the discrete anisotropic  
 7 radiative transfer (DART) model on the retrieval of spruce  
 8 stand LAI. In: 9th International Symposium on Physical  
 9 Measurements and Signatures in Remote Sensing  
 10 (ISPMSRS), Beijing, 17–19 October 2005. Beijing:  
 11 ISPRS WG VII/1, 3pp
- 12 Malenovský Z, Ufer C, Lhotakova Z, Clevers JGPW,  
 13 Schaepman ME, Albrechtova J, Cudlin P (2006) A new  
 14 hyperspectral index for chlorophyll estimation of a forest  
 15 canopy: area under curve normalised to maximal band  
 16 depth between 650–725 nm, EARSeL eProceedings, vol.  
 17 5(2), pp. 161–72
- 18 Malenovský Z, Martin E, Homolová L, Gastellu-Etchegorry  
 19 J-P, Zurita-Milla R, Schaepman ME, Pokorný R, Clevers  
 20 JGPW, Cudlín P (2008) Influence of woody elements of a  
 21 Norway spruce canopy on nadir reflectance simulated by  
 22 the DART model at very high spatial resolution. Remote  
 23 Sens Environ 112: 1–18
- 24 Martin E (2006) DART: Modèle 3D Multispectral et Inver-  
 25 sion d’Images Optiques de Satellite – Application aux  
 26 couverts forestiers. PhD thesis. Paul Sabatier University
- 27 Masson V (2000) A physically-based scheme for the urban  
 28 energy budget in atmospheric models. Bound Layer  
 29 Meteorol 94: 357–97
- 30 Masson V, Gomes L, Pigeon G, Liousse C, Pont V,  
 31 Lagouarde J-P, Voogt JA, Salmond J, Oke TR, Legain  
 32 D, Garrouste O, Lac C, Connan O, Briottet X, Lachérade S  
 33 (2007) The canopy and aerosol particles interaction in  
 34 toulouse urban layer (CAPITOU) experiment. Meteorol  
 35 Atmos Phys, this issue
- 36 North PRJ (1996) Three-dimensional forest light inter-  
 37 action model using a Monte Carlo method. IEEE  
 38 Trans Geosci Remote Sens 34: 946–56
- 39 Pinel V, Gastellu-Etchegorry JP (1998) Sensitivity of tex-  
 40 ture of high resolution images of forest to biophysical  
 41 and acquisition parameters. Remote Sens Environ 65:  
 42 61–85
- 43 Pinty B, Gobron N, Widlowski JL, Gerstl SAW, Verstraete  
 44 MM, Antunes M, Bacour C, Gascon F, Gastellu-  
 45 Etchegorry JP, Jacquemoud S, North P, Qin W, Thompson  
 46 R (2001) Radiation transfer model intercomparaison  
 47 (RAMI) exercise. J Geophys Res 106: D11, 11937–56
- 48 Pinty B, Widlowski J-L, Taberner M, Gobron N, Verstraete  
 49 MM, Disney M, Gascon F, Gastellu J-P, Jiang L, Kuusk A,  
 50 Lewis P, Li X, Ni-Meister W, Nilson T, North P, Qin W,  
 51 Su L, Tang S, Thompson R, Verhoef W, Wang H, Wang J,  
 52 Yan G, Zang H (2004) RAdiation transfer Model Intercom-  
 53 parison (RAMI) exercise: results from the second phase. J  
 54 Geophys Res 109: D06210; DOI: 10.1029/2003JD004252
- 55 Sillon FX, Arvo JR, Westin SH, Greenberg DP (1991) A  
 56 global illumination solution for general reflectance dis-  
 57 tributions. Comput Graph 25: 187–96
- 58 Soux CA, Voogt JA, Oke TR (2004) A model to calculate  
 59 what a remote sensor ‘sees’ of an urban surface. Bound  
 60 Layer Meteorol 111: 109–32
- 61 Thompson RL, Goel NS (1998) Two models for rapidly  
 62 calculating bidirectional reflectance: Photon spread (Ps)  
 63 model and statistical photon spread (SPS) model. Remote  
 64 Sens Rev 16: 157–207
- 65 Voogt JA, Oke TR (1998) Effects of urban surface geometry  
 66 on remotely sensed surface temperature. Int J Remote  
 67 Sens 19: 895–920
- 68 Voogt JA, Oke TR (2003) Thermal remote sensing of urban  
 69 climates. Remote Sens Environ 86: 370–84
- 70 Widlowski JL, Taberner M, Pinty B, Bruniquel-Pinel V,  
 71 Disney M, Fernandes R, Gastellu-Etchegorry J-P, Gobron  
 72 N, Kuusk A, Lavergne T, Leblanc S, Lewis PE, Martin E,  
 73 Mottus M, North PRJ, Qin W, Robustelli M, Rochdi N,  
 74 Ruiloba R, Soler C, Thompson R, Verhoef W, Verstraete  
 75 MM, Xie D (2007) The third RAdiation transfer Model  
 76 Intercomparison (RAMI) exercise: Documenting progress  
 77 in canopy reflectance models. J Geophys Res 112:  
 78 D09111; DOI: 10.1029/2006JD007821
- 79 Widlowski J-L, Robustelli M, Disney M, Gastellu-  
 80 Etchegorry J-P, Lavergne T, Lewis P, North PRJ, Pinty  
 81 B, Thompson R, Verstraete MM (2008) The RAMI On-  
 82 line Model Checker (ROMC): a web-based benchmarking  
 83 facility for canopy reflectance models. Remote Sens  
 84 Environ 112: 1144–50